Research Square

Preprints are preliminary reports that have not undergone peer review.
They should not be considered conclusive, used to inform clinical practice,
or referenced by the media as validated information.

Cofilin1 palmitoylation restrains metastasis by enhancing Ser3 phosphorylation and reducing protein turnover

Eryan Kong

eykong@xxmu.edu.cn

Institute of Psychiatry and Neuroscience https://orcid.org/0000-0002-4086-1441

Hesheng Kong

Universiti Sains Malaysia

Jiangli Zhu

State Key Laboratory of Biotherapy and Cancer Center https://orcid.org/0000-0002-7467-4484

Shuang Liu

The First Affiliated Hospital of Henan Medical University

Birou Lai

Universiti Sains Malaysia

Shiyi Song

The First Affiliated Hospital of Henan Medical University

Jiateng Zhong

Xinxiang Medical University https://orcid.org/0000-0003-0822-2815

Tingmin Chang

Xinxiang Medical University

Dong Guo

The First Affiliated Hospital of Henan Medical University

Jian Gao

Anhui University of Science and Technology

Badrul Yahaya

Universiti Sains Malaysia

xiao hong kang

Xinxiang Medical University

Article

Keywords: Cofilin1, Palmitoylation, Phosphorylation, Protein Stability, PPT1/2, Tumor Metastasis

Posted Date: November 11th, 2026

DOI: https://doi.org/10.21203/rs.3.rs-11303881/v1

License: This work is licensed under a Creative Commons Attribution 4.0 International License.
Read Full License

Additional Declarations: (Not answered)

Title

Cofilin1 palmitoylation restrains metastasis by enhancing Ser3 phosphorylation and reducing protein turnover

Authors

Hesheng Kong[1, 2†], Jiangli Zhu[3†], Shuang Liu[3†], Birou Lai[1, 2†], Shiyi Song[3], Jiateng Zhong[3], Tingmin Chang[3], Dong Guo[3], Jian Gao[5*], Eryan Kong[1, 3*], Badrul Hisham Yahaya[2*], Xiaohong Kang[1*]

Affiliations

[1], Department of Oncology, Longhua Hospital, Shanghai University of Traditional Chinese Medicine, Shanghai, 200032, China;

[2], Department of Biomedical Sciences, Advanced Medical and Dental Institute, Universiti Sains Malaysia, Bertam Kepala Batas, Penang, 13200, Malaysia;

[3], Henan Key Laboratory of the Prevention and Treatment of Gastrointestinal Cancer, The First Affiliated Hospital of Henan Medical University, Xinxiang 453100, China;

[4], Department of Urology, State Key Laboratory of Biotherapy and Cancer Center, West China Hospital, Sichuan University and National Collaborative Innovation Center, Chengdu, 610041, China;

[5], School of Medicine, Anhui Province Engineering Laboratory of Occupational Health and Safety, Anhui University of Science and Technology, Huainan, 232001, China;

†, equally contributed

* Corresponding author

kxhhgd@163.com

Badrul Hisham Yahaya, badrul@usm.my

Jian Gao, gaojian@aust.edu.cn

Eryan Kong: eykong2012@163.com

Abstract

Cofilin1 is a regulator of actin dynamics, governing cellular protrusion, migration, and invasion. Although its activity is modulated by phosphorylation, the functional relevance of other post-translational modifications, particularly palmitoylation, has remained unexplored. Here, we show that Cofilin1 undergoes palmitoylation, which governs its stability and Ser3 phosphorylation. Elevated levels of palmitoylated Cofilin1 (palm-Cofilin1) correlate with reduced migratory and invasive capacity. We identify PPT1 and PPT2 as the depalmitoylating enzymes of Cofilin1, with DHHC1 and DHHC2 serving as its palmitoylating counterparts. To exploit this regulation, we developed a small-molecule inhibitor targeting PPT1/2. Treatment with this inhibitor increased palm-Cofilin1 levels and suppressed tumor cell migration and invasion both in vitro and in vivo. Collectively, these findings establish palmitoylation as a pivotal regulatory axis controlling Cofilin1 stability and activity, thereby linking post-translational crosstalk to actin cytoskeleton remodeling and tumor progression. Targeting the PPT1/2–Cofilin1 axis therefore represents a compelling therapeutic strategy against tumor metastasis.

Keywords: Cofilin1; Palmitoylation; Phosphorylation; Protein Stability; PPT1/2; Tumor Metastasis

Introduction

Cofilin1, a phylogenetically conserved actin-binding protein, is a key regulator of actin filament dynamics and cytoskeletal reorganization[1,2]. By severing aged actin filaments and accelerating monomer recycling, cofilin1 drives the rapid actin turnover essential for fundamental cellular processes—including cell migration, invasion, adhesion, and morphogenesis[3-6]. Critically, dysregulation of cofilin1 activity is a hallmark of cancer pathogenesis, where it promotes aberrant cytoskeletal remodeling that underpins invasive and metastatic phenotypes[6-10]. Consequently, targeting the cofilin1-actin cytoskeletal axis represents a mechanistically rational strategy to disrupt tumor cell motility and metastasis[6,10,11]. However, translating this strategy into clinical applications has proven challenging. Direct inhibition of Cofilin1 remains unachievable, and alternative approaches—such as LIM kinase (LIMK) inhibition via LX7101, or targeting upstream regulators like Rho-associated kinase (ROCK)—have faced developmental setbacks. Moreover, the essential role of actin dynamics in normal physiological processes poses a significant risk of systemic toxicity[12,13], and selective inhibition within tumor tissue has yet to be realized. Overcoming these limitations necessitates innovative strategies that bypass direct cytoskeletal disruption.

Among PTMs governing cofilin[14-16], phosphorylation (e.g., LIMK, TESK1) at Ser3 is the best-characterized regulatory mechanism[17,18]. This modification serves as a principal molecular switch, inhibiting cofilin1's actin-severing activity by impairing filament binding. Reactivation occurs via dephosphorylation by specific phosphatases (e.g., slingshot, chronophin, PP1/2A)[19-21]. The precise equilibrium between cofilin1 phosphorylation and dephosphorylation is thus critical for spatiotemporal control of actin dynamics and associated cellular behaviors[22]. Alterations in this balance are implicated in cancer progression, with context-dependent effects: heightened Ser3 phosphorylation can stabilize actin networks and suppress motility in some settings[23-25], while reduced phosphorylation often correlates with enhanced invasion and metastasis[26]. Despite its established role, targeting phospho-regulation presents inherent complexities due to pathway redundancy and the pleiotropic effects of kinase/phosphatase modulation[27].

Beyond phosphorylation, the functional contributions of other PTMs to Cofilin1 regulation remain largely unexplored. Among these, protein palmitoylation—a reversible lipid modification involving the attachment of palmitate to cysteine residues via a thioester bond—has emerged as a critical regulatory mechanism for numerous proteins[28-30]. This modification is dynamically regulated: catalyzed by palmitoyltransferases (PATs, specifically DHHC family members 1-9 and 11-25, excluding DHHC10) and reversed by protein thioesterases (including APT1/2, PPT1/2, and ABHD17s)[31,32]. Significantly, we identify dynamic palmitoylation as a novel regulatory layer for cofilin1, dramatically influencing its phosphorylation status at Ser3. Using human cervical cancer (HeLa) models, we demonstrate that palmitoylated cofilin1 (palm-cofilin1) correlates with suppressed migratory and invasive capacities.

To leverage this discovery therapeutically while circumventing the limitations of direct cytoskeletal targeting, we propose an alternative axis: PPT1/2-mediated depalmitoylation of cofilin1. By employing a rationally designed inhibitor of the thioesterases PPT1/2, we selectively enhanced palm-cofilin1 levels. This intervention significantly impeded tumor cell migration and invasion in vitro and attenuated tumor progression in vivo. Collectively, these findings establish the PPT1/2-cofilin1 palmitoylation axis as a tractable and therapeutically viable target for disrupting metastasis-prone cytoskeletal dynamics, offering a promising strategy to overcome the translational hurdles associated with conventional cofilin1-actin targeting.

Results

Elevated Cofilin1 Expression Correlates with Poor Prognosis in Multiple Cancers and Undergoes Palmitoylation at Multiple Sites

Our investigation commenced with an assessment of Cofilin1 expression profiles across various cancer types using The Cancer Genome Atlas (TCGA) datasets. This analysis revealed frequent upregulation of Cofilin1 in multiple tumor types (Fig. 1A). Furthermore, Kaplan-Meier survival analysis demonstrated a significant inverse correlation between elevated Cofilin1 protein levels and reduced patient survival—a trend particularly evident in cervical, hepatocellular, and lung carcinomas (Fig. 1B). This observation was corroborated by comparative analysis of mRNA levels, which indicated significant upregulation of Cofilin1 in various carcinomas relative to their respective normal tissues (Fig. S1A-S1C). Moreover, Cofilin1 mRNA levels remained elevated across distinct tumor stages (I-IV) when compared to normal tissue controls (Fig. S1D-S1F). These findings collectively suggest a potentially crucial role for Cofilin1 in promoting tumor progression across diverse cancer types.

To validate the palmitoylation status of Cofilin1, we next examined its expression and modification in relevant cancer cell lines derived from cervical, hepatocellular, and lung carcinomas. These analyses confirmed abundant Cofilin1 expression and palmitoylation level in these cells (Fig. S1G). Given these results, the HeLa cell line (human cervical carcinoma) was selected as a representative model for subsequent mechanistic studies investigating the role of Cofilin1 palmitoylation in vitro. Using the Acyl-RAC assay, we assessed both ectopically and endogenously expressed Cofilin1. The results confirmed that Cofilin1 undergoes robust palmitoylation both in vitro and in vivo (Fig. 1C and Fig. S1H). Furthermore, treatment with 2-Bromopalmitate (2-BP), a known inhibitor of protein palmitoylation,

resulted in a consistent decrease in palmitoylated Cofilin1 levels in Cofilin1-expressing cells (Fig. 1D), indicating that this modification is dynamic and reversible.

Sequence alignment subsequently identified four evolutionarily conserved cysteine residues (C39, C80, C139, C147) as potential palmitoylation sites on Cofilin1 (Fig. 1E). To determine the specific sites of modification, Flag-tagged Cofilin1 was purified and subjected to mass spectrometry (MS) analysis. The MS data confirmed that all four cysteine residues were palmitoylated, as evidenced by the characteristic mass shift of +238 Da[28,33] (Fig. 1F and Fig. S2A-S2C). Functional studies employing site-directed mutagenesis were then conducted. Mutating Cysteine-80 to Alanine (C80A) resulted in a significant reduction in palmitoylated Cofilin1 levels compared to wild-type (WT) protein (Fig. 1G-1H). Notably, the quadruple mutation (4CA, C39A/C80A/C139A/C147A) completely abrogated Cofilin1 palmitoylation (Fig. 1I-1J). Interestingly, the 4CA mutation was also associated with a noticeable decrease in total Cofilin1 protein level, suggesting a potential link between palmitoylation status and protein stability (Fig. 1I-1J).

Collectively, these findings establish a strong correlation between elevated Cofilin1 expression and poor prognosis in multiple cancer types, while highlighting the functional significance of palmitoylation at multiple conserved cysteine residues, which may influence Cofilin1 stability.

Palmitoylation Modulates the Protein Stability of Cofilin1

The observed reduction in total Cofilin1 protein level following mutations at the 4CA sites (Fig. 1I) prompted a focused investigation into the potential role of palmitoylation in regulating Cofilin1 expression or stability. To first assess whether altered mRNA transcription contributes to this effect, total mRNA was extracted from cells expressing WT or mutant Cofilin1. Quantitative real-time PCR (qRT-PCR) analysis revealed no significant difference in Cofilin1 mRNA levels between the WT and mutant constructs (Fig. S2D), suggesting that post-transcriptional mechanisms, specifically protein stability, are likely modulated by palmitoylation.

To directly evaluate protein stability, cycloheximide (CHX) chase experiments were performed in HeLa cells expressing WT or mutant Cofilin1. These experiments demonstrated that the stability of the C80A mutant was significantly impaired compared to WT Cofilin1, whereas single mutations at C39A, C139A, or C147A did not exhibit this effect (Fig. 2A-2B). Notably, the 4CA mutant displayed an even more pronounced reduction in stability compared to C80A, indicating a cumulative effect of palmitoylation at multiple sites on Cofilin1 protein stability (Fig. 2A-2B).

Further support for the role of palmitoylation in maintaining Cofilin1 stability was obtained using 2-BP. Treatment with 2-BP in HeLa cells resulted in a significant decrease in the stability of endogenous Cofilin1 (Fig. 2C), reinforcing the conclusion that palmitoylation is crucial for its stability.

To elucidate the degradation pathway involved, various inhibitors targeting distinct protein degradation routes were employed. The results indicated that MG132, an inhibitor of the proteasome pathway, effectively blocked the accelerated degradation of both C80A and 4CA mutants (Fig. 2D), suggesting

their clearance occurs via the ubiquitin-proteasome system. Coimmunoprecipitation (Co-IP) assays, performed by coexpressing Cofilin1 and its mutants with Ubiquitin-Ha, provided further validation. These assays demonstrated elevated ubiquitination levels for the C80A and 4CA mutants compared to WT Cofilin1 (Fig. 2E).

In summary, these findings provide compelling evidence that palmitoylation critically regulates the protein stability of Cofilin1. Mechanistically, reduced palmitoylation appears to enhance Cofilin1 ubiquitination, subsequently accelerating its degradation via the proteasome pathway.

Dynamic Cofilin1 Palmitoylation is Regulated by PPT1/2 and DHHC1/2

To identify enzymes involved in Cofilin1 depalmitoylation, we coexpressed various protein thioesterases (APT1/2, PPT1/2, and ABHD17a) alongside Cofilin1 in HeLa cells. Our analysis revealed that coexpression of either PPT1 or PPT2 significantly reduced the levels of palmitoylated Cofilin1 (Fig. 3A-3B). To corroborate these findings, we generated PPT1-knockout (KO) and PPT2-KO cell lines. Consistent with the overexpression experiments, depletion of either PPT1 or PPT2 resulted in elevated levels of palmitoylated Cofilin1. Notably, the loss of PPT2 exhibited a more pronounced effect on increasing palmitoylation levels compared to PPT1 deficiency (Fig. 3C), suggesting PPT2 is the principal enzyme responsible for Cofilin1 depalmitoylation.

Furthermore, we demonstrated a direct interaction between PPT2 and Cofilin1 through immunoprecipitation assays in HeLa cells (Fig. 3D). Regarding its impact on protein stability, PPT2 expression was found to significantly accelerate the degradation of Cofilin1 compared to control conditions (Fig. 3E-3F).

Conversely, to elucidate the enzymes promoting Cofilin1 palmitoylation, we coexpressed various DHHC proteins with Cofilin1 in HeLa cells. The results indicated that expression of DHHC1, DHHC2, or DHHC8 notably increased the abundance of palmitoylated Cofilin1 (Fig. 3G). Furthermore, to assess the functional consequences for protein stability, we coexpressed these DHHC enzymes with Cofilin1 in HeLa cells treated with CHX. Interestingly, while DHHC1 and DHHC2 significantly enhanced Cofilin1 protein stability, DHHC8 did not exhibit this effect (Fig. 3H-3K).

Collectively, these findings establish that the dynamic palmitoylation of Cofilin1 is regulated by PPT1/2 and DHHC1/2, and this post-translational modification critically modulates the protein stability of Cofilin1.

Cofilin1 Palmitoylation Positively Correlates with Ser3 Phosphorylation

Given that phosphorylation at Ser3 serves as a critical functional switch for Cofilin1, regulating its activity and interaction with actin, we next sought to investigate the potential crosstalk between Cofilin1 palmitoylation and its Ser3 phosphorylation status. To this end, we examined phospho-Cofilin1 (S3) levels under conditions where palmitoylation levels were experimentally modulated. Notably, our results indicated that mutations at C39A, C80A, or 4CA resulted in significantly diminished phospho-Cofilin1 (S3) levels, whereas mutations at C139A or C147A did not exhibit this effect (Fig. 4A-4B). Consistent

with this observation, coexpression of PPT2, an enzyme known to reduce palmitoylation levels (Fig. 3A-3D), also markedly decreased phospho-Cofilin1 (S3) abundance (Fig. 4A-4B). These findings suggest a positive correlation between reduced palmitoylation and attenuated Ser3 phosphorylation of Cofilin1.

Previous studies within this investigation, as depicted in Figures 2A-2B, demonstrated that the C80A and 4CA mutations significantly decrease the overall protein level of Cofilin1 (Fig. 4C). Acknowledging this potential confounding factor, we normalized phospho-Cofilin1 (S3) levels to the total Cofilin1 protein levels. This normalization revealed that the C80A mutant specifically impaired Ser3 phosphorylation, independent of its effect on total protein abundance (Fig. 4D).

Conversely, to explore the impact of increased palmitoylation, we examined the effect of coexpressing DHHC1 or DHHC2, which are known to enhance palmitoylation. This manipulation led to a notable elevation in phospho-Cofilin1 (S3) levels (Fig. 4E-4F), further supporting the link between palmitoylation status and Ser3 phosphorylation.

Finally, to explore the possibility of a feedback loop originating from Ser3 phosphorylation to regulate palmitoylation, we introduced mutations at the Ser3 site, substituting it with alanine (S3A, mimicking non-phosphorylation) or aspartic acid (S3D, mimicking constitutive phosphorylation). Intriguingly, neither mutation affected the level of palmitoylated Cofilin1 (Fig. 4G-4H). This observation suggests that the regulatory influence of palmitoylation on Ser3 phosphorylation in Cofilin1 may operate unidirectionally, without a reciprocal feedback mechanism from phosphorylation to palmitoylation levels.

Dynamic Cofilin1 Palmitoylation Modulates Migration and Invasion in HeLa Cells

To elucidate the role of Cofilin1 in HeLa cells and the functional consequences of its palmitoylation status, we generated Cofilin1-knockout (Cofilin1-KO) cells (Fig. S3A-S3E). Our findings indicated that cell proliferation remained unaffected (Fig. 5A), whereas cell migration, assessed via wound healing assay (Fig. 5B-5C), and invasion, evaluated using Transwell assay (Fig. 5D-5E), were significantly suppressed in Cofilin1-KO cells compared to WT HeLa cells. This underscores Cofilin1's essential role in these dynamic cellular processes.

To further assess the impact of palmitoylation on Cofilin1 function, we rescued Cofilin1-KO cells with either WT or mutant forms of Cofilin1. Notably, expression of the C80A mutant and the double mutation (C39A/C80A, designated 2CA) significantly enhanced cell migration and invasion relative to the control rescue, whereas neither the C39A mutant nor WT Cofilin1 exhibited this effect (Fig. 5F-5G, 5H-5I). The rationale for utilizing the 2CA mutant instead of a quadruple mutant (4CA) was based on protein stability considerations; the 4CA mutant exhibited markedly reduced protein stability (Fig. S3F), potentially confounding functional analysis. Importantly, the 2CA mutant maintained moderate expression levels and induced Cofilin1 activation (as indicated by Ser3 phosphorylation) to a similar extent as the 4CA mutant (Fig. S3F). Collectively, these data suggest that the regulation of cell migration and invasion is contingent upon the palmitoylation status of Cofilin1, with reduced palmitoylation leading to increased activity and potentially hyperactive migration/invasion behavior.

Additionally, we manipulated the endogenous palmitoylation status of Cofilin1 in WT HeLa cells by transfecting them with constructs encoding PPT1/2 or DHHC1/2. The results demonstrated that co-expression of PPT1/2 significantly enhanced cell migration and invasion in HeLa cells (Fig. 5J-5K). Conversely, expression of DHHC1 or DHHC2 significantly impaired cell migration and invasion (Fig. 5L, 5M-5N).

In summary, these findings underscore the critical role of Cofilin1 palmitoylation in mediating its cellular functions, particularly migration and invasion. Furthermore, they suggest that modulating Cofilin1 palmitoylation levels presents a potential therapeutic strategy for inhibiting these processes.

Targeting PPT1/2 to Enhance Cofilin1 Palmitoylation as a Therapeutic Strategy for Suppressing Cell Migration and Invasion

To investigate the therapeutic potential of enhancing Cofilin1 palmitoylation, we aimed to develop selective inhibitors targeting the active site of PPT2[34], the primary Cofilin1 depalmitoylating enzyme identified in our study. We employed a structure-based virtual screening strategy, emphasizing conformational compatibility between candidate ligands and the enzyme's binding site. Initially, approximately 1.6 million compounds from the library were filtered using Lipinski's Rule of Five to ensure favorable drug-like properties. A two-step molecular docking protocol was subsequently applied to prioritize potential binders, followed by clustering analysis and manual selection, ultimately yielding 34 representative compounds. These candidates were evaluated in HeLa cells using a RAC activity assay to assess their capacity to modulate Cofilin1 palmitoylation. Among these, compound L471-1746, designated as Targeting PPT2 (TPPT), emerged as the most potent candidate (Fig. S4).

Computational modeling indicated that TPPT exhibits favorable binding interactions within the active site of PPT2 (Fig. 6A). Notably, the model also suggested potential binding within the active site of PPT1 (Fig. S5A), indicating that TPPT may possess dual inhibitory activity against both PPT1 and PPT2 (Fig. S5B). Experimental validation confirmed that TPPT treatment significantly increases Cofilin1 palmitoylation levels while concomitantly elevating Ser3 phosphorylation (Fig. 6B–6C). At the cellular level, TPPT treatment in HeLa cells led to reduced endogenous Cofilin1 protein stability (Fig. 6D), a decrease in the number of filopodia and membrane protrusions (Fig. 6E), and dose-dependent suppression of both cell migration and invasion (Fig. 6F–6G, 6H–6I).

Furthermore, a substantial and dose-dependent inhibition of HeLa cell proliferation was observed following treatment with TPPT (Fig. 6J). Complementary mRNA sequencing analysis indicated a pronounced downregulation of the PI3K-AKT signaling pathway at the transcriptomic level (Fig. S6). While the impact on proliferation was notable, it occurred in parallel with more pronounced effects on cell migration and invasion. This suggests that the suppression of these latter processes may represent a primary mechanism of action of TPPT, particularly in the context of tumor progression.

Collectively, these findings provide compelling evidence that enhancing Cofilin1 palmitoylation through the inhibition of PPT1/2 represents a promising therapeutic strategy for attenuating tumor cell

proliferation, migration, and invasion, thereby justifying further investigation into its potential clinical applications.

Targeting PPT1/2 with TPPT suppresses tumor growth and metastasis by modulating actin cytoskeleton dynamics at the cellular leading edge

Analysis of clinical samples revealed that Cofilin1 levels are generally elevated in tumor tissues compared to adjacent normal controls (Fig. 1A). Concomitantly, Cofilin1 palmitoylation is significantly reduced (Fig. S7A), correlating with increased PPT1/2 expression levels (Fig. S7B-S7C). Furthermore, Kaplan-Meier survival analysis using TCGA datasets demonstrated a significant negative correlation between elevated PPT1/2 levels and reduced patient survival across various carcinomas, including liver and lung cancers (Fig. S8A-S8B). These observations suggest that targeting PPT1/2 holds therapeutic potential for intervening in multiple cancer types.

In subcutaneous tumor mouse models (Fig. S9A), TPPT treatment significantly inhibited the growth of HeLa cells (Fig. 7A). Notably, similar treatment also suppressed the growth of other tumor cell lines, including A549 (lung cancer) and Huh7 (liver cancer) (Fig. S9C-S9D), indicating broader efficacy across diverse tumor types. Moreover, in a liver xenograft model (Fig. S9B), TPPT treatment not only suppressed tumor growth but also inhibited the metastasis of HeLa cells (Fig. 7B). Analysis of tumor tissues dissected from the liver showed that TPPT treatment upregulated both Cofilin1 palmitoylation and S3 Cofilin1 phosphorylation compared to the control group (Fig. 7C).

Mechanistically, live cell imaging of HeLa cells expressing GFP-Cofilin1 revealed dynamic interactions with the actin cytoskeleton (labeled with SiR-actin 652) at the leading edge under control conditions. TPPT treatment impaired this dynamicity, resulting in the retraction of membrane protrusions (Fig. 7D). Consistent with this, deletion of Cofilin1 in HeLa cells nearly abolished actin cytoskeleton dynamics (Fig. S10A). Rescuing WT Cofilin1 in Cofilin1-KO cells restored actin dynamics (Fig. S10B), whereas rescuing the Cofilin1-2CA variant further enhanced this dynamicity (Fig. S10C). These findings suggest that increasing Cofilin1 palmitoylation negatively modulates actin dynamics at the leading edge, potentially inhibiting filopodia formation and tumor cell migration.

Collectively, these data indicate that reduced Cofilin1 palmitoylation in cervical tumors may be associated with elevated PPT1/2 levels. Targeting PPT1/2 using TPPT suppresses both the growth of various tumor cells and the metastasis of HeLa cells, likely through modulation of actin cytoskeleton dynamics at the cellular leading edge.

Discussion

This study furnishes comprehensive evidence establishing a direct link between Cofilin1 palmitoylation and tumor progression, while identifying an unknown therapeutic strategy centered on the PPT1/2-Cofilin1 axis. Initial analyses leveraging TCGA data consistently revealed elevated Cofilin1 expression across diverse cancer types, correlating strongly with adverse patient prognosis. This observation aligns with the well-documented role of Cofilin1 in modulating cytoskeletal dynamics, cell motility, and invasion[5-10]—processes integral to tumor metastasis. Subsequent confirmation of Cofilin1 palmitoylation

in cancer cell lines, coupled with the identification of four evolutionarily conserved palmitoylation sites, provided the foundation for investigating the functional relevance of this post-translational modification.

Our findings demonstrate that Cofilin1 palmitoylation is dynamically regulated by PPT1/2, which functions as a critical molecular switch. Specifically, PPT1/2 promotes the downregulation of palmitoylated Cofilin1, concomitantly reducing its protein stability and phosphorylation levels. The latter effect directly augments Cofilin1 activity, thereby enhancing actin cytoskeleton dynamics. This culminates in the maintenance of extended, motile filopodia at the cellular leading edge, ultimately facilitating tumor metastasis. Conversely, TPPT, a specifically developed dual PPT1/2 inhibitor, effectively reverses this cascade. It attenuates actin cytoskeleton dynamics, results in shortened and rigid filopodia, and consequently suppresses tumor progression and metastasis (Fig. 7E).

A central finding is that palmitoylation critically regulates Cofilin1 protein stability, as demonstrated by reduced levels in the C80A mutant and complete instability in the 4CA mutant, implicating multiple palmitoylation sites. CHX chase experiments and 2-BP treatment confirmed that palmitoylation status directly influences Cofilin1 turnover, primarily via the ubiquitin-proteasome system. This post-translational control mechanism represents a novel layer of Cofilin1 regulation, distinct from transcriptional control[35] and potentially enabling rapid modulation of its levels in response to cellular signals.

The identification of PPT1/2 as key regulators of Cofilin1 depalmitoylation and DHHC1/2 as palmitoylating enzymes provides crucial mechanistic insight. The finding that PPT2 depletion had a more pronounced effect on Cofilin1 palmitoylation than PPT1 depletion suggests PPT2 may be the dominant enzyme in this context, although the potential dual inhibition of PPT1/2 by TPPT warrants further investigation into the relative contributions of each enzyme in different cellular contexts or cancer types. Conversely, the identification of DHHC1 and DHHC2 as palmitoylating enzymes not only completes the enzymatic landscape governing Cofilin1 palmitoylation but also links increased palmitoylation to enhanced protein stability, consistent with our earlier findings. This enzymatic interplay establishes a dynamic regulatory circuit for Cofilin1 function.

Critically, we identified an unprecedented hierarchical relationship: palmitoylation acts upstream of Ser3 phosphorylation. Enhanced palm-cofilin1 elevates inhibitory phosphorylation, while reduced palmitoylation decreases it. This positions palmitoylation as a master regulator that coordinates both cofilin1 stability and activity.

Functional validation in cofilin1-KO rescue models confirmed that palmitoylation-deficient mutants (C80A/2CA) exhibit hypermigratory phenotypes. This directly correlates with reduced Ser3 phosphorylation and excessive actin remodeling—mirroring the pro-metastatic effects of PPT1/2 overexpression. Conversely, DHHC1/2 expression or TPPT treatment recapitulates the palm-cofilin1-stabilized, phosphorylation-enhanced state that suppresses motility.

Conventional strategies targeting the cofilin1-actin axis face significant translational hurdles, including

dose-limiting toxicity from disruption of essential actin functions in normal physiology[12,13], compensatory reactivation by phosphatases (e.g., slingshot, chronophin, PP1/2A)[19-21], pleiotropic effects of upstream kinase inhibitors (LIMK/ROCK), and absence of clinical-stage cofilin1-specific agents[11,36]. Our discovery of the PPT1/2-cofilin1 palmitoylation axis addresses these limitations by establishing a novel regulatory node upstream of phosphorylation, enabling indirect modulation of actin dynamics without direct cytoskeletal disruption, and offering enhanced specificity through enzyme-substrate targeting. The translational promise of this axis is demonstrated by TPPT—a rationally designed PPT1/2 inhibitor that significantly elevates palm-cofilin1 and inhibitory Ser3 phosphorylation, suppresses migration/invasion across multiple carcinoma lineages (HeLa, A549, Huh7), inhibits primary tumor growth and metastasis in vivo, and mechanistically attenuates leading-edge actin dynamics. Clinical relevance is further evidenced in patient tumors showing elevated cofilin1 expression with reduced palmitoylation and increased PPT1/2 levels correlating with poor survival outcomes.

Notably, PPT1/2 may exhibit broader enzymatic substrates beyond cofilin1[28,37], potentially facilitating modulation of the PI3K-AKT signaling cascade to suppress tumor cell proliferation. While this polypharmacology may confer beneficial effects for clinical applications, the underlying mechanisms warrant further investigation.

Collectively, this work fundamentally redefines cofilin1 biology by establishing palmitoylation as a critical regulator of protein stability and activity, mapping the PPT1/2-DHHC1/2 enzymatic circuit, and revealing hierarchical control wherein palmitoylation governs Ser3 phosphorylation. The efficacy of TPPT validates PPT1/2 as a druggable node, demonstrating that modulating this axis offers a clinically viable strategy distinct from conventional approaches. Future efforts should prioritize developing isoform-selective PPT inhibitors, elucidating palmitoylation-phosphorylation crosstalk mechanisms, validating this strategy in patient-derived xenograft models of therapy-resistant malignancies, and identifying predictive biomarkers for patient stratification. Collectively, this paradigm shift from direct cytoskeletal disruption toward precision targeting of cofilin1 palmitoylation opens new avenues for progression and metastasis interception therapeutics.

Declarations

Competing interests

HSK, JLZ, XHK, and EYK are listed as inventors on a pending patent regarding the targeting of PPT as an intervention strategy for treating tumors. All other authors declare no competing interests.

Authors' contributions

Conceptualization: BHY, XHK, JG, JLZ, EYK; Methodology: HSK, SL, BRL, SYS, JTZ, TMC, DG, EYK; Investigation: HSK, SL, BRL, SYS, DG; Visualization: SYS, TMC, EYK; Supervision: BHY, XHK, JG, JLZ, EYK; Writing—original draft: XHK, JG, JLZ, EYK; Writing—review & editing: BHY, XHK, JG, JLZ, EYK.

Funding

This study was supported by funding granted by the National Natural Science Foundation of China

32371309. Henan Science and Technology Research Project 242102310117. Henan Provincial Medical Science and Technology Research Project LHGJ20260556.

Availability of data and materials

Further information and requests for resources and reagents should be directed to and will be fulfilled by the Lead Contact, Eryan Kong (eykong2012@163.com). All reagents generated in this study are available from the Lead Contact with a completed Materials Transfer Agreement.

Materials and Methods

Animal care and human tissue acquisition

Immunodeficient nude female mice (BALB/c genotype) were procured from Charles River Laboratories (Beijing, China) and maintained under specific pathogen-free (SPF) conditions. Housing parameters included a controlled temperature (25°C), a 12-hour light/dark cycle, ad libitum access to food and water, and group housing. Human cervical cancer specimens and paired adjacent normal tissues were obtained from surgical resections conducted at the First Affiliated Hospital of Xinxiang Medical University. All patients provided signed informed consent prior to enrollment, had received no prior chemotherapy or radiotherapy, and were fully informed of the study parameters. Fresh tissue samples were processed for immunohistochemical analysis by the hospital's Department of Pathology. This study received full ethical oversight. The human research protocol was approved by the Xinxiang Medical University Institutional Review Board (Approval Code: XYLL-20250413), adhering to the Declaration of Helsinki. The animal experimental protocol was approved by the Xinxiang Medical University Animal Ethics Committee (Approval ID: XYLL-20250413), complying with National Institutes of Health standards for laboratory animal welfare and institutional ethical guidelines. All procedures strictly followed approved protocols for acquisition, handling, and experimentation.

Cell Culture, Transfection, and Chemical Treatments

All cell lines were obtained from the American Type Culture Collection (ATCC). Cells were cultured under standard conditions (37°C, 5% CO_2) in media supplemented with 10% fetal bovine serum (FBS; Gibco, USA), 100 U/mL penicillin, and 100 μg/mL streptomycin. Culture media specifications were as follows: HEK293T, HepG2, and MHCC97H cells: High-glucose DMEM (Gibco, USA); HeLa cells: High-glucose MEM (Gibco, USA); A549, H1299, and H260 cells: RPMI-1640 (Gibco, USA). Transient transfections were performed using Lipofectamine 3000 (Invitrogen) and Opti-MEM (Life Technologies) according to the manufacturer's instructions. Following a 6-hour transfection period, complexes were replaced with complete growth medium, and cells were incubated for an additional 24 hours prior to analysis. For chemical treatments, cells at 70–80% confluence were exposed to: 2-Bromohexadecanoic acid (2-BP; Sigma-Aldrich, Cat# 238422); Dimethyl sulfoxide (DMSO; vehicle control; Sigma-Aldrich, Cat# D8418).

Plasmid Construction

All expression plasmids were generated using the In-Fusion HD cloning system. Murine cofilin1 (ENSG00000172757) and human PPT1/PPT2 cDNAs were amplified by RT-PCR and initially cloned into pUC19 for sequence verification. Following validation, these cDNAs were

directionally subcloned into a modified pCMV3 vector to generate N-terminal Flag-tagged constructs for mammalian expression. The generated constructs included wild-type murine cofilin1, single cysteine-to-alanine point mutants (C39A, C80A, C139A, C147A), combinatorial mutants (C39A/C80A and C39A/C80A/C139A/C147A), and human PPT1 and PPT2. Gene-specific primers were designed for all subcloning procedures. All final expression constructs were verified by bidirectional Sanger sequencing prior to experimental use.

Acetyl-Resin-Assisted Capture Assay (Acyl-RAC)

The Acyl-RAC assay was performed to specifically enrich S-palmitoylated proteins via hydroxylamine-dependent thioester cleavage and thiol-affinity capture[28,37]. Cells or tissues were lysed in RIPA buffer (20 mM Tris-HCl pH 7.5, 150 mM NaCl, 1% Triton X-100) containing protease inhibitors, followed by sonication (3 × 10-sec pulses) and centrifugation (15,000 ×g, 10 min, 4°C). Protein concentrations were quantified using the BCA assay. For each assay, 1 mg of lysate was treated with 50 mM N-ethylmaleimide (NEM) in blocking buffer (100 mM HEPES, 1 mM EDTA, 2.5% SDS, pH 7.5) at 50°C for 1 hour to alkylate free thiols. Proteins were precipitated with 3 volumes of cold acetone, washed four times with 70% acetone, and resuspended in 600 µL binding buffer (100 mM HEPES, 1 mM EDTA, 1% SDS, pH 7.5). Samples were divided into two parallel treatments: experimental samples received 2 M neutralized hydroxylamine (HA, pH 7.0) to cleave thioester bonds, while control samples received 2 M NaCl. Thiopropyl Sepharose 6B beads (50 µL) were added to each reaction, followed by rotation at room temperature for 4 hours. Beads were washed five times with binding buffer, and bound proteins were eluted with Laemmli buffer at 42°C for 15 minutes prior to SDS-PAGE and immunoblotting with target-specific antibodies. Untreated samples and hydroxylamine-free controls were included to verify palmitoylation dependence.

mPEG-Maleimide-Based Palmitoylation Detection

Protein S-palmitoylation was detected using a mPEG-Mal labeling protocol[29]. Briefly, 500 µg of protein lysate was reduced with 10 mM tris (2-carboxyethyl) phosphine (TCEP; 30 min, RT), followed by alkylation of free cysteines with 25 mM NEM (2 hr, RT). NEM activity was quenched via three sequential methanol-chloroform-water (4:1.5:3) extractions. Residual solvents were removed by centrifugal evaporation (Labconco Centrivap). The dried pellet was reconstituted in 100 µL TEA buffer (50 mM triethanolamine, 150 mM NaCl, 1× protease inhibitors, pH 7.3) containing 4% SDS, then incubated at 37°C for 10 minutes with agitation. Thioester cleavage was initiated by adding 1 M neutralized hydroxylamine (1 hr, RT). Proteins were reprecipitated and redissolved in 30 µL TEA buffer with 4% SDS and 4 mM EDTA (37°C). For maleimide-PEG conjugation, samples were adjusted to 0.2% Triton X-100 in 90 µL TEA buffer and incubated with 1.33 mM mPEG-Mal (10 mM final concentration) for 2 hours at RT. Reactions were terminated by precipitation, and pellets were solubilized in Laemmli buffer (Bio-Rad) for immunoblot analysis.

Metabolic labeling of palmitate and click chemistry

Click chemistry was performed as previous described[31]. Cultured HeLa cells incubated with 50 µM 17-ODYA (Cayman Chemical, Cat#90270) for 8h at 37°C. DMSO acted as control. Cells were washed with PBS and lysed in lysis buffer (50 mM Tris-HCl, pH 7.4, 150 mM NaCl, 0.1% TritonX-100, 0.1% SDS). 12000 rpm for 10 min at 4°C. The cell lysates were used for click chemistry. For Cu2+-catalyzed click reaction: aliquot (94µl) lysates were incubated with 1µl of 10 mM biotin-azide stock in DMSO, 2µl of 50 mM TECP, 1µl of 10 mM TBTA stock in DMSO, 2µl of 50 mM CuSO4 stock in H2O at room temperature (RT) for 1h. 0.2µl of 10 mM EDTA was added to terminate the reaction. Biotinylated (palmitoylated) proteins were affinity isolated using 25µl streptavidin beads at RT for 4h and analyzed by WB using Flag antibody.

Protein Purification for Mass Spectrometric Analysis

HEK-293T cells were transfected with pCMV3-Flag-Cofilin1 using Lipofectamine 3000 and incubated for 24 hours to establish stable expression. Transfected cells were lysed in buffer (20 mM Tris pH 7.5, 150 mM NaCl, 1% Triton X-100) supplemented with protease inhibitor cocktail (Roche). Lysates were clarified through two sequential centrifugations (15,000 ×g, 10 min, 4°C), and supernatants were subjected to affinity purification using Anti-DYKDDDDK resin (Sino Biological, #101274-MM13-T). Following pre-equilibration with PBS (10 mM, pH 7.4), the resin was incubated with lysates overnight at 4°C with rotation. Bound resin was collected by centrifugation and washed three times with PBS. Target protein elution was performed using 100 mM glycine buffer (10 mM NaCl, pH 3.0). Eluted Flag-Cofilin1 was quantified via Coomassie blue staining (Beyotime, #P0017) prior to downstream analysis.

Mass Spectrometric Analysis of Cofilin1 Palmitoylation

Purified Flag-Cofilin1 (30 μg) was digested using the Filter-Aided Sample Preparation (FASP) protocol. Proteins were reduced with 2 mM TCEP and alkylated with 10 mM iodoacetamide (IAA) before transfer to 10-kDa molecular weight cutoff filters. Sequential washes were performed with 8 M urea and 50 mM Tris-HCl (pH 6.8) at 13,000 ×g (20°C). Proteolytic digestion was conducted with GluC (New England Biolabs, P8100S) at 1:50 (w/w) enzyme-to-substrate ratio in 1× reaction buffer (37°C, 16 hours). Peptides were recovered by centrifugation, lyophilized, and stored at -80°C. LC-MS/MS analysis was performed on an Orbitrap Fusion Lumos mass spectrometer (Thermo Fisher Scientific) coupled to an EasyNano LC 1000 system (Thermo Fisher Scientific). Peptides were separated using either a homemade C18 column (3 μm, 75 μm × 15 cm), or a commercial C4 column (5 μm, 75 μm × 15 cm) with a flow rate of 600 nL/min. Both systems employed 60-minute linear gradients from 3% to 90% solvent B (0.1% formic acid in acetonitrile). MS acquisition operated in data-dependent mode with the following parameters: MS1 scan range m/z 350–1550 (120K resolution; AGC target 4×10^5); MS2 scans (30K resolution; AGC target 1×10^5; 1.6 Th isolation window); dynamic exclusion 15 s. Complementary fragmentation techniques included higher-energy collisional dissociation (HCD, 32 eV) and electron-transfer/higher-energy collision dissociation (EThcD, 25 eV), with ETD reaction times automatically optimized. Database searches were performed using Byonic v2.16.11 (Protein Metrics) with semi-specific GluC cleavage (≤3 missed cleavages), precursor mass tolerance of 20 ppm, and fragment mass tolerance of 50 ppm. Variable modifications included methionine oxidation, asparagine/glutamine deamidation, cysteine carbamidomethylation, N-terminal acetylation, and cysteine palmitoylation (+238.2297 Da). High-confidence identifications required automated filtering (Byonic score ≥ 200) with manual verification of diagnostic b/y ion series continuity.

Immunohistochemical Staining

Formalin-fixed, paraffin-embedded tumor specimens were sectioned and processed for immunohistochemical analysis. Tissue sections were incubated with primary antibodies followed by biotin-conjugated anti-rabbit IgG secondary antibody. Antigen-antibody complexes were visualized using a 3,3'-diaminobenzidine (DAB) detection system. Immunoreactivity was quantified using a validated 12-point scoring system as previously established. Samples were stratified into high-expression (score ≥ 4) and low-expression (score 0-3) categories based on predetermined thresholds.

Immunofluorescence Staining and Imaging

Cells were plated on poly-D-lysine-coated coverslips and transfected with designated plasmids. At 24 hours post-transfection, cells were fixed with 4% paraformaldehyde (Electron Microscopy Sciences, #15710) and permeabilized with 0.1% Triton X-100 in PBS. Non-specific binding sites were blocked with 3% bovine serum albumin (BSA) in PBS. Sequential incubations were performed with primary antibodies against Flag (Sigma-Aldrich, #F7425; 1:500) and HA (Sino Biological, #10028-MM10; 1:500), followed by species-matched secondary antibodies conjugated to Alexa Fluor 488 (Thermo Fisher Scientific, #A11034; 1:500) and Alexa Fluor 594 (Thermo Fisher Scientific, #A21135; 1:500). Coverslips were mounted using DAPI-Fluoromount-G (Electron Microscopy Sciences, #17984-24) for nuclear counterstaining. Fluorescence images were acquired using a Leica TCS SP8 STED microscope with optimized detector configurations.

Live cell imaging

HeLa cells were cultured in glass bottom cell culture dish (NEST, 801001). GFP, GFP-Cofilin1 or GFP-Cofilin1-2CA was transfected into HeLa cells using Lipofectamine 3000 at 70% confluency. SiR-actin Kit (Spirochrome, SC001) was used to stain live F-actin, Abs/Em:652/674nm and 488/495nm were used for imaging. Scan mode, xyt. Magnification, 63×. Time interval=1. Focus system, Adaptive Focus Control.

CRISPR/Cas9-Mediated Cofilin1 Knockout in HeLa Cells

Single-guide RNAs (sgRNAs) targeting exonic regions of Cofilin1 (ENSG00000172757) were designed using the CRISPOR algorithm. Oligonucleotides incorporating BbsI restriction sites were synthesized by Shanghai Bioligo Biotechnology (Shanghai, China). The pX458 vector was digested with BbsI (New England Biolabs, R3539), ligated to annealed sgRNAs, and transformed into DH5α competent cells (Beijing Protein Innovation, Beijing, China). Positive clones were selected via ampicillin resistance, validated by Sanger sequencing (Wuhan Genecreate Biological Engineering), and maxiprepped using the Tiangen Plasmid Kit (Tiangen Biotech, Beijing, China). HeLa cells were transfected with two distinct sgRNA constructs using Lipofectamine™ 3000 (Thermo Fisher Scientific). At 48 hours post-transfection, GFP-positive single cells were isolated by fluorescence-activated cell sorting (FACS; BD FACSAria™ III, BD Biosciences) into 96-well plates. Monoclonal colonies were expanded for 14 days, followed by genomic DNA extraction. Knockout efficiency was confirmed through PCR amplification of target loci and bidirectional Sanger sequencing.

Wound Healing Assay

Cell migration was assessed using ibidi Culture-Insert 2-well chambers (Ibidi, #80206) according to manufacturer specifications. Briefly, 2.5×10^5 cells in 100 μL complete medium were seeded per chamber well and incubated at 37°C/5% CO_2 until confluent (24 hours). Following insert removal with sterile forceps, standardized wounds were established. Chambers were replenished with fresh MEM containing 0.5% FBS to minimize proliferation-dependent migration. Wound closure was documented at 0, and 24-hour intervals through phase-contrast imaging (Nikon Eclipse Ti). Migration kinetics were quantified by measuring residual wound width using ImageJ software (NIH), with data expressed as

percentage closure relative to t=0.

Transwell Migration and Invasion Assays

Cell motility was evaluated using 6.5-μm pore Transwell chambers (Corning). For migration assays, 1×10^5 serum-starved cells in 100 μL MEM were seeded in upper chambers, with 500 μL MEM/10% FBS as chemoattractant in lower compartments. After 24-hour incubation (37°C/5% CO_2), non-migrated cells were removed by cotton swab. Migrated cells were fixed in 4% PFA, stained with 0.1% crystal violet (Sigma), and quantified in five random 20× fields (Nikon Eclipse E200). For invasion assays, Transwell inserts were pre-coated with Matrigel™ (BD Biosciences; 1:8 dilution, 200 μg/cm²). Cells were processed identically to migration assays but incubated for 48 hours. All experiments included triplicate wells and were independently replicated three times.

Lentiviral Packaging in HEK293T Cells

Lentiviral particles were produced by co-transfecting HEK293T cells with 20 μg of transfer plasmid and 15 μg of packaging plasmids (pSPAX2:pMD2.G at 3:1 ratio). Viral supernatants were harvested 36 hours post-transfection, clarified through 0.45-μm filtration, and concentrated by ultracentrifugation (70,000 × g, 2 h, 4°C). Alternatively, unconcentrated supernatants were aliquoted and stored at -80°C for direct applications.

Generation of Luciferase-Expressing HeLa Stable Cell Line

HeLa cells were transduced with lentiviral particles encoding firefly luciferase and mCherry-puromycin resistance cassettes (Hanbio Biotechnology). At 48 hours post-transduction, cell populations were expanded under continuous puromycin selection (2 μg/mL) for 7 days to establish stable polyclones. Stable genomic integration was confirmed through three orthogonal validation methods: fluorescence microscopy for mCherry expression detection, and quantitative bioluminescence imaging using the IVIS Spectrum CT platform (PerkinElmer) following intraperitoneal D-luciferin administration (150 mg/kg).

Molecular docking based -virtual screening

To identify small-molecule inhibitors targeting the active site of PPT2 (PDB ID: 1PJA[34]), a structure-based virtual screening strategy was employed. The initial screening library consisted of approximately 1.6 million commercially available compounds from the ChemDiv database. To ensure favorable drug-like properties, all compounds were first filtered using Lipinski's Rule of Five, resulting in a refined subset of approximately 1.06 million candidates. Molecular docking was performed using Sybyl-X 2.1 software (Tripos, USA) following a two-step screening protocol. In the first stage, a rapid docking approach was applied by adjusting conformational parameters to accelerate the screening process, yielding approximately 10,600 compounds with preliminary binding potential. This was followed by a standard precision docking procedure using default parameters to rigorously evaluate binding affinities, from which the top 500 candidates were retained. Subsequently, structural clustering was conducted to eliminate redundant chemotypes among the high-scoring hits. A total of 34 representative compounds were ultimately selected for further biological evaluation to assess their potential to modulate PPT2 enzymatic activity. In addition, target molecule was also docked into the active site of PPT1 to investigate its potential binding interactions. The crystal structure of PPT1 (PDB ID: 3GRO) was retrieved from the

Protein Data Bank and prepared using Sybyl-X 2.1, including removal of water and ligands, hydrogen addition, and protonation state assignment. The 3D structure of the compound was generated from its 2D representation and energy-minimized using the Tripos force field. Docking into the active site was performed using the Surflex-Dock module with binding pockets defined by the Protomol tool. Results were assessed based on docking scores and key interactions, and visualized using PyMOL 2.5.

Subcutaneous Xenograft Mouse Model

Four-to-five-week-old Balb/c female nude mice (Charles River Laboratories) were housed under specific pathogen-free conditions (22 ± 1°C, 12-hour light/dark cycles) with all procedures approved by the Institutional Animal Care and Use Committee. HeLa cells were maintained in MEM supplemented with 10% FBS and 1% penicillin-streptomycin (37°C, 5% CO_2). During logarithmic growth phase at 70–80% confluence, cells were trypsinized, neutralized with complete medium, and centrifuged (300 × g, 5 min). Cell pellets were resuspended in sterile PBS at 1×10^7 cells/mL. Following dorsal flank disinfection with povidone-iodine/70% ethanol, 100 μL suspensions containing 1×10^6 cells were injected subcutaneously using 27-gauge needles with superficial deposition confirmed by visual bleb formation. Animals were individually housed with ad libitum access to food/water. Tumor dimensions were measured twice weekly with digital calipers, and volumes calculated as (length × width^2) × 0.5.

Orthotopic Liver Implantation Model

Female Balb/c nude mice (4–5 weeks old, n=8/group) were anesthetized via intraperitoneal injection of pentobarbital sodium (120 μL of 0.1% solution). Following midline laparotomy under aseptic conditions, the left hepatic lobe was externalized. HeLa cells stably expressing firefly luciferase (1×10^6 cells in 100 μL serum-free PBS) were slowly injected into the parenchyma using a 30-gauge insulin syringe to prevent capsular rupture. The abdominal wall was closed with 6-0 vicryl sutures and skin with wound clips. Postoperative analgesia (buprenorphine, 0.1 mg/kg) was administered every 12 hours for 48 hours. Successful engraftment was confirmed at day 10 via bioluminescence imaging (IVIS Spectrum CT; PerkinElmer) following intraperitoneal D-luciferin administration (150 mg/kg). Animals were subsequently randomized to experimental cohorts.

Statistical Analysis

Basic descriptive data are presented as means ± standard errors of means (SEM). Statistical analyses were carried out using GraphPad Prism software. Statistical significance for two groups was determined by unpaired two-tailed Student's t-test. For determining differences between more than two groups, one-way ANOVA followed by Tukey's post-hoc tests were used. Statistical significance mentioned with * represents significant differences. Statistical significance was defined as: ns, not significant, *$p < 0.05$, **$p < 0.01$ and ***$p < 0.001$. The n value is reported as the number of cells or mice per group from at least 3 replicate experiments.

References

1. Nishida, E., Maekawa, S., and Sakai, H. (1984). Cofilin, a protein in porcine brain that binds to actin filaments and inhibits their interactions with myosin and tropomyosin. Biochemistry ***23***, 5307-5313, 10.1021/bi00317a032.
2. Bamburg, J.R., Harris, H.E., and Weeds, A.G. (1980). Partial purification and characterization of an actin

depolymerizing factor from brain. FEBS letters ***121***, 178-182, 10.1016/0014-5793(80)81292-0.
3. Schneider, F., Duong, T.A., Metz, I., et al. (2021). Mutual functional dependence of cyclase-associated protein 1 (CAP1) and cofilin1 in neuronal actin dynamics and growth cone function. Progress in neurobiology ***202***, 102050, 10.1016/j.pneurobio.2021.102050.
4. Rehklau, K., Hoffmann, L., Gurniak, C.B., et al. (2017). Cofilin1-dependent actin dynamics control DRP1-mediated mitochondrial fission. Cell Death Dis ***8***, e3063, 10.1038/cddis.2017.448.
5. Goode, B.L., Eskin, J., and Shekhar, S. (2023). Mechanisms of actin disassembly and turnover. The Journal of cell biology ***222***, 10.1083/jcb.202309021.
6. Chen, L., Cai, J., Huang, Y., et al. (2020). Identification of cofilin-1 as a novel mediator for the metastatic potentials and chemoresistance of the prostate cancer cells. Eur J Pharmacol ***880***, 173100, 10.1016/j.ejphar.2020.173100.
7. Sidani, M., Wessels, D., Mouneimne, G., et al. (2007). Cofilin determines the migration behavior and turning frequency of metastatic cancer cells. The Journal of cell biology ***179***, 777-791, 10.1083/jcb.200707009.
8. Oser, M., Yamaguchi, H., Mader, C.C., et al. (2009). Cortactin regulates cofilin and N-WASp activities to control the stages of invadopodium assembly and maturation. The Journal of cell biology ***186***, 571-587, 10.1083/jcb.200812176.
9. Delorme-Walker, V., Seo, J.Y., Gohla, A., et al. (2015). Chronophin coordinates cell leading edge dynamics by controlling active cofilin levels. Proceedings of the National Academy of Sciences of the United States of America ***112***, E5150-5159, 10.1073/pnas.1510945112.
10. Collazo, J., Zhu, B., Larkin, S., et al. (2014). Cofilin drives cell-invasive and metastatic responses to TGF-β in prostate cancer. Cancer research ***74***, 2362-2373, 10.1158/0008-5472.Can-13-3058.
11. Dahlstroem, C., Paraschiakos, T., Sun, H., and Windhorst, S. (2023). Cryo-EM structures of actin binding proteins as tool for drug discovery. Biochem Pharmacol ***214***, 115680, 10.1016/j.bcp.2023.115680.
12. Lee, M.H., Kundu, J.K., Chae, J.I., and Shim, J.H. (2019). Targeting ROCK/LIMK/cofilin signaling pathway in cancer. Arch Pharm Res ***42***, 481-491, 10.1007/s12272-019-01153-w.
13. Berabez, R., Routier, S., Bénédetti, H., et al. (2022). LIM Kinases, Promising but Reluctant Therapeutic Targets: Chemistry and Preclinical Validation In Vivo. Cells ***11***, 10.3390/cells11132090.
14. Weng, W., Gu, X., Yang, Y., et al. (2023). N-terminal α-amino SUMOylation of cofilin-1 is critical for its regulation of actin depolymerization. Nature communications ***14***, 5688, 10.1038/s41467-023-41520-2.
15. Pignataro, M., Di Rocco, G., Lancellotti, L., et al. (2020). Phosphorylated cofilin-2 is more prone to oxidative modifications on Cys39 and favors amyloid fibril formation. Redox Biol ***37***, 101691, 10.1016/j.redox.2020.101691.
16. Vogl, A.M., Phu, L., Becerra, R., et al. (2020). Global site-specific neddylation profiling reveals that NEDDylated cofilin regulates actin dynamics. Nat Struct Mol Biol ***27***, 210-220, 10.1038/s41594-019-0370-3.
17. Bamburg, J.R. (1999). Proteins of the ADF/cofilin family: essential regulators of actin dynamics. Annual review of cell and developmental biology ***15***, 185-230, 10.1146/annurev.cellbio.15.1.185.
18. Bamburg, J.R., and Bernstein, B.W. (2008). ADF/cofilin. Current biology : CB ***18***, R273-275, 10.1016/j.cub.2008.02.002.
19. Bernstein, B.W., and Bamburg, J.R. (2010). ADF/cofilin: a functional node in cell biology. Trends Cell Biol ***20***, 187-195, 10.1016/j.tcb.2010.01.001.
20. Agnew, B.J., Minamide, L.S., and Bamburg, J.R. (1995). Reactivation of phosphorylated actin depolymerizing factor and identification of the regulatory site. The Journal of biological chemistry ***270***, 17582-17587, 10.1074/jbc.270.29.17582.
21. Kanellos, G., and Frame, M.C. (2016). Cellular functions of the ADF/cofilin family at a glance. Journal of cell science ***129***, 3211-3218, 10.1242/jcs.187849.
22. Wang, W., Eddy, R., and Condeelis, J. (2007). The cofilin pathway in breast cancer invasion and metastasis.

Nature reviews. Cancer ***7***, 429-440, 10.1038/nrc2148.
23. Mardilovich, K., Gabrielsen, M., McGarry, L., et al. (2015). Elevated LIM kinase 1 in nonmetastatic prostate cancer reflects its role in facilitating androgen receptor nuclear translocation. Mol Cancer Ther ***14***, 246-258, 10.1158/1535-7163.Mct-14-0447.
24. Yoshioka, K., Foletta, V., Bernard, O., and Itoh, K. (2003). A role for LIM kinase in cancer invasion. Proceedings of the National Academy of Sciences of the United States of America ***100***, 7247-7252, 10.1073/pnas.1232344100.
25. Davila, M., Frost, A.R., Grizzle, W.E., and Chakrabarti, R. (2003). LIM kinase 1 is essential for the invasive growth of prostate epithelial cells: implications in prostate cancer. The Journal of biological chemistry ***278***, 36868-36875, 10.1074/jbc.M306196200.
26. Wang, Y., Kuramitsu, Y., Kitagawa, T., et al. (2015). Cofilin-phosphatase slingshot-1L (SSH1L) is over-expressed in pancreatic cancer (PC) and contributes to tumor cell migration. Cancer Lett ***360***, 171-176, 10.1016/j.canlet.2015.02.015.
27. Shah, K., and Cook, M. (2023). LIMK2: A Multifaceted kinase with pleiotropic roles in human physiology and pathologies. Cancer Lett ***565***, 216207, 10.1016/j.canlet.2023.216207.
28. Yuan, W., Lu, L., Rao, M., et al. (2021). GFAP hyperpalmitoylation exacerbates astrogliosis and neurodegenerative pathology in PPT1-deficient mice. Proceedings of the National Academy of Sciences of the United States of America ***118***, 10.1073/pnas.2022261118.
29. Liu, H., Yan, P., Wu, C., et al. (2023). Palmitoylated Sept8-204 modulates learning and anxiety by regulating filopodia arborization and actin dynamics. Sci Signal ***16***, eadi8645, 10.1126/scisignal.adi8645.
30. Zhou, B., Hao, Q., Liang, Y., and Kong, E. (2023). Protein palmitoylation in cancer: molecular functions and therapeutic potential. Mol Oncol ***17***, 3-26, 10.1002/1878-0261.13308.
31. Yan, P., Liu, H., Zhou, T., et al. (2022). Crosstalk of Synapsin1 palmitoylation and phosphorylation controls the dynamicity of synaptic vesicles in neurons. Cell Death Dis ***13***, 786, 10.1038/s41419-022-05235-4.
32. Anam, Z., Kumari, G., Mukherjee, S., et al. (2022). Complementary crosstalk between palmitoylation and phosphorylation events in MTIP regulates its role during Plasmodium falciparum invasion. Front Cell Infect Microbiol ***12***, 924424, 10.3389/fcimb.2022.924424.
33. Gottlieb, C.D., Zhang, S., and Linder, M.E. (2015). The Cysteine-rich Domain of the DHHC3 Palmitoyltransferase Is Palmitoylated and Contains Tightly Bound Zinc. The Journal of biological chemistry ***290***, 29259-29269, 10.1074/jbc.M115.691147.
34. Calero, G., Gupta, P., Nonato, M.C., et al. (2003). The crystal structure of palmitoyl protein thioesterase-2 (PPT2) reveals the basis for divergent substrate specificities of the two lysosomal thioesterases, PPT1 and PPT2. The Journal of biological chemistry ***278***, 37957-37964, 10.1074/jbc.M301225200.
35. Heib, T., Hermanns, H.M., Manukjan, G., et al. (2021). RhoA/Cdc42 signaling drives cytoplasmic maturation but not endomitosis in megakaryocytes. Cell reports ***35***, 109102, 10.1016/j.celrep.2021.109102.
36. Sousa-Squiavinato, A.C.M., and Morgado-Díaz, J.A. (2024). A glimpse into cofilin-1 role in cancer therapy: A potential target to improve clinical outcomes? Biochim Biophys Acta Rev Cancer ***1879***, 189087, 10.1016/j.bbcan.2024.189087.
37. Ma, Y., Yuan, X., Wei, A., et al. (2024). Enhancing Gpx1 palmitoylation to inhibit angiogenesis by targeting PPT1. Redox Biol ***77***, 103376, 10.1016/j.redox.2024.103376.

Figure legends

Fig. 1. Elevated Cofilin1 Expression Correlates with Poor Prognosis in Multiple Cancers and Undergoes Multisite Palmitoylation

(A) Analysis of Cofilin1 mRNA levels across diverse cancer types utilizing TCGA datasets.

(B) Kaplan-Meier survival analysis demonstrating the association between elevated Cofilin1 expression and reduced patient survival in cervical, hepatocellular, and lung carcinomas.

(C) Detection of palmitoylation on both ectopically and endogenously expressed Cofilin1 via Acyl-RAC assay.
(D) Assessment of Cofilin1 palmitoylation by Acyl-RAC assay in HeLa cells following exposure to the palmitoylation inhibitor 2-BP.
(E) Evolutionary conservation analysis of cysteine residues in Cofilin1 via multispecies protein sequence alignment.
(F) Identification of palmitoylation sites by mass spectrometry, revealing a characteristic +238 Da mass shift on cysteine residues in purified Cofilin1.
(G–H) Evaluation of palmitoylation levels by Acyl-RAC assay (G) and quantification (H) for WT Cofilin1 and cysteine-to-alanine point mutants expressed in HeLa cells.
(I–J) Evaluation of palmitoylation levels by Acyl-RAC assay (I) and quantification (J) for WT Cofilin1 and a multi-cysteine mutant (4CA) expressed in HeLa cells.
Blots are representative; data represent mean ± SEM (n=3 biological replicates). Statistical significance: *p ≤ 0.05, **p ≤ 0.01 (Student's t-test or one-way ANOVA with Tukey's post hoc test).

Fig. 2. Palmitoylation Regulates Cofilin1 Protein Stability
(A–B) Assessment of Cofilin1-Flag and mutant protein levels by immunoblotting (A) and quantification (B) in HeLa cells treated with cycloheximide (CHX) to inhibit protein synthesis.
(C) Quantification of Cofilin1-Flag protein levels in HeLa cells co-treated with CHX and 2-BP.
(D) Evaluation of Cofilin1-Flag and mutant protein levels in HeLa cells treated with CHX combined with inhibitors of specific protein degradation pathways.
(E) Analysis of Cofilin1 ubiquitination levels by immunoprecipitation in HeLa cells co-expressing Cofilin1 (or mutants) with ubiquitin-HA and treated with the proteasome inhibitor MG132.
Blots are representative; data represent mean ± SEM (n=3 biological replicates). Statistical significance: *p ≤ 0.05, **p ≤ 0.01 (Student's t-test or one-way ANOVA with Tukey's post hoc test).

Fig. 3. Dynamic Palmitoylation of Cofilin1 is Modulated by PPT1/2 and DHHC1/2
(A–B) Evaluation of Cofilin1-Flag palmitoylation by Acyl-RAC assay (A) and quantification (B) in HEK293T cells co-expressing candidate thioesterases (APT1/2, PPT1/2, ABHD17a).
(C) Analysis of Cofilin1-Flag palmitoylation levels in WT, PPT1-KO, and PPT2-KO HEK293T cells.
(D) Co-immunoprecipitation assay demonstrating the interaction between Cofilin1-Flag and PPT2-HA in HeLa cells.
(E–F) Assessment of Cofilin1 protein levels by immunoblotting (E) and quantification (F) in HeLa cells expressing Cofilin1 ± PPT2 and treated with CHX.
(G) Screening of DHHC palmitoyltransferases modulating Cofilin1-Flag palmitoylation via Acyl-RAC assay in HEK293T cells.
(H–K) Assessment of Cofilin1 protein levels by immunoblotting (H) and quantification (I–K) in HeLa cells expressing Cofilin1 ± DHHC1, DHHC2, or DHHC8 and treated with CHX.
Blots are representative; data represent mean ± SEM (n=3 biological replicates). Statistical significance: *p ≤ 0.05, **p ≤ 0.01 (Student's t-test or one-way ANOVA with Tukey's post hoc test).

Fig. 4. Cofilin1 Palmitoylation Positively Correlates with Ser3 Phosphorylation
(A-D) Evaluation of palmitoylation levels by Acyl-RAC assay (A) and quantification (B-D) for WT Cofilin1 ± PPT2, and cysteine-to-alanine point mutants expressed in HeLa cells.
(E-F) Assessment of Cofilin1 S3 phosphorylation levels by immunoblotting (E) and quantification (F) in HeLa cells expressing Cofilin1 ± DHHC1, DHHC2, or DHHC8.
(G-H) Evaluation of Cofilin1-Flag palmitoylation by Acyl-RAC assay (G) and quantification (H) in

HeLa cells expressing WT Cofilin1 or Cofilin1-S3A, Cofilin1-S3D mutants.
Blots are representative; data represent mean ± SEM (n=3 biological replicates). Statistical significance: *p ≤ 0.05, **p ≤ 0.01, ***p ≤ 0.001, ****p ≤ 0.0001 (one-way ANOVA with Tukey's post hoc test).

Fig. 5. Dynamic Cofilin1 Palmitoylation Modulates Migration and Invasion in HeLa Cells
(A) Cell viability was assessed in WT and Cofilin1-KO HeLa cells using CCK-8 assays.
(B–C) Migratory capacity of WT and Cofilin1-KO HeLa cells was evaluated by wound healing assay (B), with quantification of relative wound width percentage (C).
(D-E) Matrigel invasion analysis of WT and Cofilin1-KO HeLa cells (D), with quantification (E).
(F-G) Wound healing analysis of Cofilin1-KO HeLa cells rescued with WT or Cofilin1 mutants (F), with quantification (G).
(H-I) Matrigel invasion analysis of Cofilin1-KO HeLa cells rescued with WT or Cofilin1 mutants (H), with quantification (I).
(J) Wound healing analysis of HeLa cells expressing empty vector or PPT1/2, with quantification.
(K) Matrigel invasion analysis of HeLa cells expressing empty vector or PPT1/2, with quantification.
(L) Wound healing analysis of HeLa cells expressing empty vector, DHHC1 or DHHC2, with quantification.
(M-N) Matrigel invasion analysis of HeLa cells expressing empty vector, DHHC1 or DHHC2 (M), with quantification (N).
Statistical significance: *p ≤ 0.05, **p ≤ 0.01, ***p ≤ 0.001 (Student's t-test or one-way ANOVA with Tukey's post hoc test).

Fig. 6. Targeting PPT1/2 to Enhance Cofilin1 Palmitoylation as a Therapeutic Strategy for Suppressing Cell Migration and Invasion
(A) Binding mode of TPPT in the active site of PPT2. PPT2 is shown as a cartoon (blue), TPPT as green sticks, and key residues as yellow sticks. Hydrogen bonds are indicated by red dashed lines.
(B) Analysis of Cofilin1 palmitoylation levels in HeLa cells treated with DMSO or TPPT, and quantified.
(C) Assessment of Cofilin1 S3 phosphorylation levels in HeLa cells treated with DMSO or TPPT, and quantified.
(D) Evaluation of Cofilin1 protein levels by immunoblotting and quantification in HeLa cells treated with CHX ± TPPT.
(E) Cultured HeLa cells treated with DMSO or TPPT were fixed for phalloidin staining and immunofluorescence imaging, and number of filopodia and major protrusions per cell were quantified.
(F-G) Wound healing analysis of HeLa cells treated with DMSO or TPPT (F), with quantification (G).
(H-I) Matrigel invasion analysis of HeLa cells treated with DMSO or TPPT (H), with quantification (I).
(J) Cell viability was assessed in HeLa cells treated with DMSO or TPPT using CCK-8 assays.
Blots are representative; data represent mean ± SEM (n=3 biological replicates). Statistical significance: *p ≤ 0.05, **p ≤ 0.01, ***p ≤ 0.001, ****p ≤ 0.0001 (Student's t-test or one-way ANOVA with Tukey's post hoc test).

Fig. 7. Targeting PPT1/2 with TPPT suppresses tumor growth and metastasis by modulating actin cytoskeleton dynamics at the cellular leading edge

(A) Tumor growth kinetics in subcutaneous xenografts (HeLa cells) treated with DMSO or TPPT (intraperitoneal injection). Tumor volumes were quantified.
(B) Metastatic burden in an orthotopic liver implantation model treated with DMSO or TPPT. Tumor weight and fluorescent metastatic signal were quantified.
(C) Tumor tissues from liver implantation mouse model were evaluated for the levels of Cofilin1 palmitoylation and S3 phosphorylation, and quantified.
(D) Live-cell imaging of HeLa cells expressing GFP-Cofilin1 and incubated with SiR-actin, pretreated with DMSO (vehicle control), followed by treatment with TPPT (10 μM).
(E) Proposed mechanistic model of PPT-Cofilin1 palmitoylation regulation in tumor progression.
Blots are representative; data represent mean ± SEM (n=3 biological replicates). Statistical significance: *p ≤ 0.05, **p ≤ 0.01, ***p ≤ 0.001, ****p ≤ 0.0001 (Student's t-test or one-way ANOVA with Tukey's post hoc test).

Fig. S1. Cofilin1 is upregulated and palmitoylated in tumor tissues
(A-C) Elevated Cofilin1 mRNA expression in cervical (A), liver (B), and lung (C) cancer tissues versus adjacent normal tissue.
(D-F) Cofilin1 mRNA levels persist across tumor stages (I-IV) in cervical (D), liver (E), and lung (F) cancers.
(G) Cofilin1 is ubiquitously expressed in varied types of cancer cell lines.
(H) Detection of palmitoylated Cofilin1 in HeLa cells via metabolic labeling with 17-ODYA, click chemistry (biotin-azide), and streptavidin enrichment. Hydroxylamine (HA) treatment confirmed thioester linkage specificity.
Blots are representative; data represent mean ± SEM. Statistical significance: **p ≤ 0.01, ***p ≤ 0.001, ****p ≤ 0.0001 (Student's t-test or one-way ANOVA with Tukey's post hoc test).

Fig. S2. Identification of Cofilin1 palmitoylation sites
(A-C) Mass spectrometry identification of palmitoylated cysteines (C80, C139, C147) via +238 Da mass shifts.
(D) mRNA expression of WT and mutant Cofilin1 constructs in HeLa cells (RT-qPCR).

Fig. S3. Generation and validation of Cofilin1-KO HeLa cells
(A) CRISPR-Cas9 targeting strategy for exon 2 deletion using dual gRNAs (gRNA1, gRNA2).
(B–C) A 112-bp deletion in the knockout allele (B), confirmed by sequencing (C).
(D–E) Genotyping (D) and immunoblot validation of Cofilin1 knockout (E).
(F) Immunoblot analysis of Ser3 phosphorylation in HeLa cells expressing WT or mutant Cofilin1 (2CA, 4CA).

Fig. S4. Structure-based virtual screening workflow for PPT2 inhibitors
Molecular docking reveals TPPT binding stably to the PPT2 active site via key interactions: hydrogen bonds (Tyr178, Leu45) and hydrophobic packing (Leu45, Val230, Ile231, Leu149). TPPT exhibits high spatial/physicochemical complementarity, supporting its potential as a selective PPT2 inhibitor.

Fig. S5. Structural basis of TPPT binding to PPT1 and PPT2

(A) TPPT (green) forms hydrogen bonds (red dashes) with PPT1 (light green; key residues: cyan).

(B) Structural overlay of TPPT-bound PPT1 (green) and PPT2 (yellow). Both enzymes share an α/β-hydrolase fold and conserved catalytic triad (PPT1: Ser115-His289; PPT2: Ser111-His283). TPPT adopts similar conformations but adjusts its terminal moiety to accommodate divergent active-site topographies (e.g., steric constraints from Met41 in PPT1 vs. flexibility near Leu45 in PPT2).

Fig. S6. TPPT modulates the PI3K-AKT pathway at the transcriptional level

RNA sequencing of HeLa cells treated with DMSO or TPPT (10 μM) identifies PI3K-AKT signaling as a downregulated pathway.

Fig. S7. Elevation of PPT1/2 in Cervical Tumor Tissues

(A) The levels of cofilin1 and its palmitoylation in cervical cancer and adjacent tissue samples were analyzed and quantified.

(B) The mRNA expression levels of PPT1/2 in cervical cancer and adjacent tissue samples were examined and quantified.

(C) The protein levels of PPT1/2 in cervical cancer and adjacent tissue samples were assessed using immunohistochemistry.

Fig. S8. Elevated PPT1/2 expression correlates with poor clinical prognosis

(A) High PPT2 expression associates with reduced survival across carcinomas (Kaplan-Meier analysis).

(B) High PPT1 expression associates with reduced survival across carcinomas (Kaplan-Meier analysis).

Fig. S9. TPPT suppresses tumor growth in xenograft models

(A) Experimental design: Subcutaneous HeLa xenograft with TPPT treatment.

(B) Experimental design: Liver xenograft with TPPT treatment.

(C) Tumor growth kinetics in subcutaneous xenografts (A549) treated with DMSO or TPPT (intraperitoneal injection). Tumor weight and volumes were quantified.

(D) Tumor growth kinetics in subcutaneous xenografts (Huh7) treated with DMSO or TPPT (intraperitoneal injection). Tumor weight and volumes were quantified.

Statistical significance: $^{**}p \leq 0.01$, $^{****}p \leq 0.0001$ (Student's t-test).

Fig. S10. Cofilin1 palmitoylation modulates actin dynamics at leading edges

(A) Live-cell imaging of Cofilin1-KO HeLa cells expressing GFP empty vector and incubated with SiR-actin.

(B) Live-cell imaging of Cofilin1-KO HeLa cells expressing GFP-Cofilin1 empty vector and incubated with SiR-actin.

(C) Live-cell imaging of Cofilin1-KO HeLa cells expressing GFP-Cofilin1-2CA empty vector and incubated with SiR-actin.

Fig. S11. Uncropped blots for Fig. 1.

Fig. S12. Uncropped blots for Fig. 2.

948 **Fig. S13. Uncropped blots for Fig. 3.**

949 **Fig. S14. Uncropped blots for Fig. 4.**

950 **Fig. S15. Uncropped blots for Fig. 6 and Fig. 7.**

Fig. 1

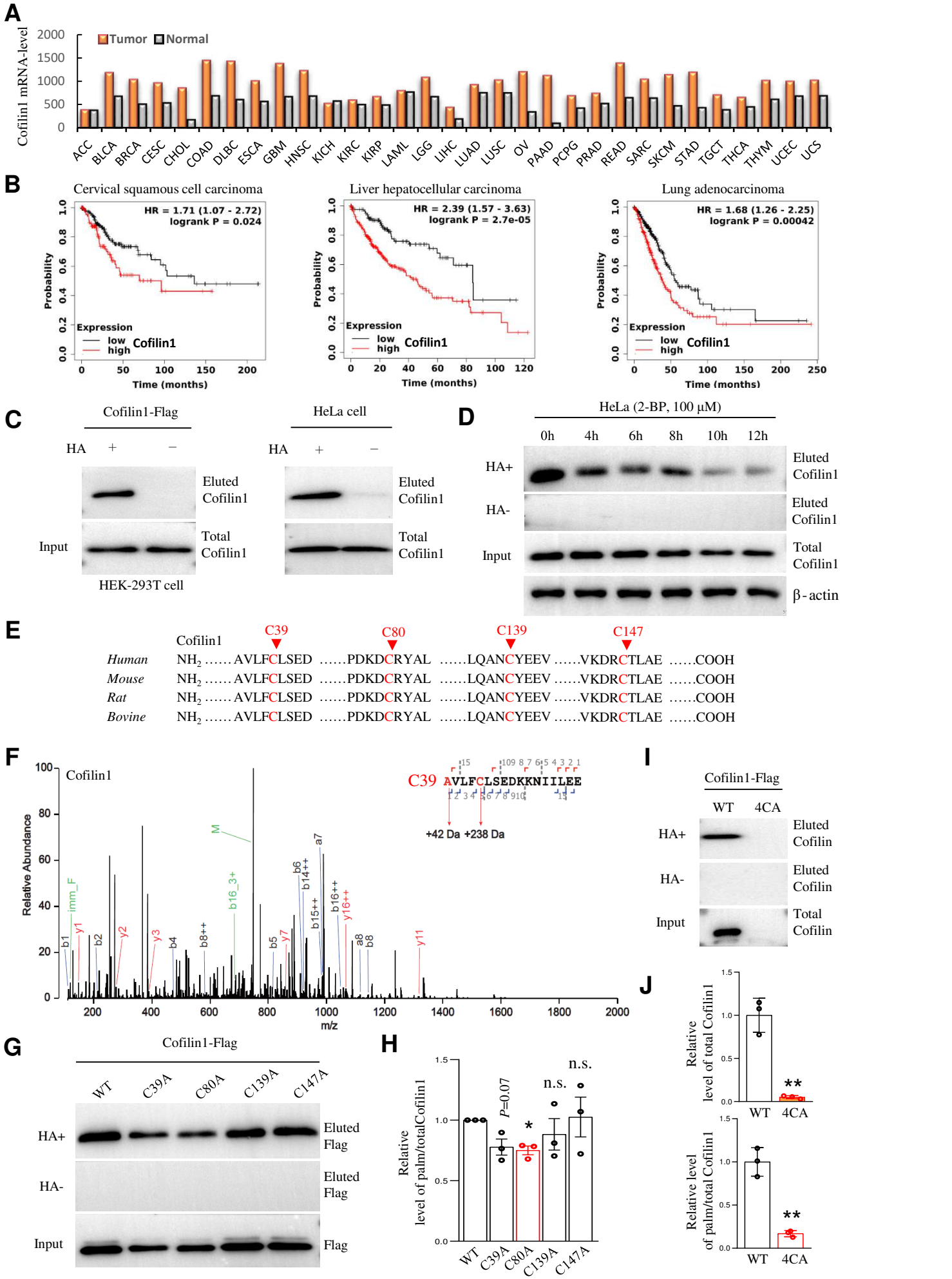

A
Cofilin1 mRNA-level
Tumor
Normal
ACC BLCA BRCA CESC CHOL COAD DLBC ESCA GBM HNSC KICH KIRC KIRP LAML LGG LIHC LUAD LUSC OV PAAD PCPG PRAD READ SARC SKCM STAD TGCT THCA THYM UCEC UCS
B
Cervical squamous cell carcinoma
HR = 1.71 (1.07 - 2.72)
logrank P = 0.024
Liver hepatocellular carcinoma
HR = 2.39 (1.57 - 3.63)
logrank P = 2.7e-05
Lung adenocarcinoma
HR = 1.68 (1.26 - 2.25)
logrank P = 0.00042
Probability
Expression
low
high
Cofilin1
Time (months)
C
Cofilin1-Flag
HeLa cell
HA
Eluted Cofilin1
Input
Total Cofilin1
HEK-293T cell
D
HeLa (2-BP, 100 μM)
0h 4h 6h 8h 10h 12h
HA+
HA-
Eluted Cofilin1
Input
Total Cofilin1
β-actin
E
Cofilin1
C39 C80 C139 C147
Human NH2 ..... AVLFCLSED ..... PDKDCRYAL ..... LQANCYEEV ..... VKDRCTLAE ..... COOH
Mouse NH2 ..... AVLFCLSED ..... PDKDCRYAL ..... LQANCYEEV ..... VKDRCTLAE ..... COOH
Rat NH2 ..... AVLFCLSED ..... PDKDCRYAL ..... LQANCYEEV ..... VKDRCTLAE ..... COOH
Bovine NH2 ..... AVLFCLSED ..... PDKDCRYAL ..... LQANCYEEV ..... VKDRCTLAE ..... COOH
F
Cofilin1
Relative Abundance
m/z
C39 AVLFCLSEDKKNIILEE
+42 Da +238 Da
I
Cofilin1-Flag
WT 4CA
HA+
HA-
Input
Eluted Cofilin
Total Cofilin
J
Relative level of total Cofilin1
Relative level of palm/total Cofilin1
WT 4CA
G
Cofilin1-Flag
WT C39A C80A C139A C147A
HA+
HA-
Input
Eluted Flag
Flag
H
Relative level of palm/totalCofilin1
P=0.07
n.s.
WT C39A C80A C139A C147A

Fig. 2

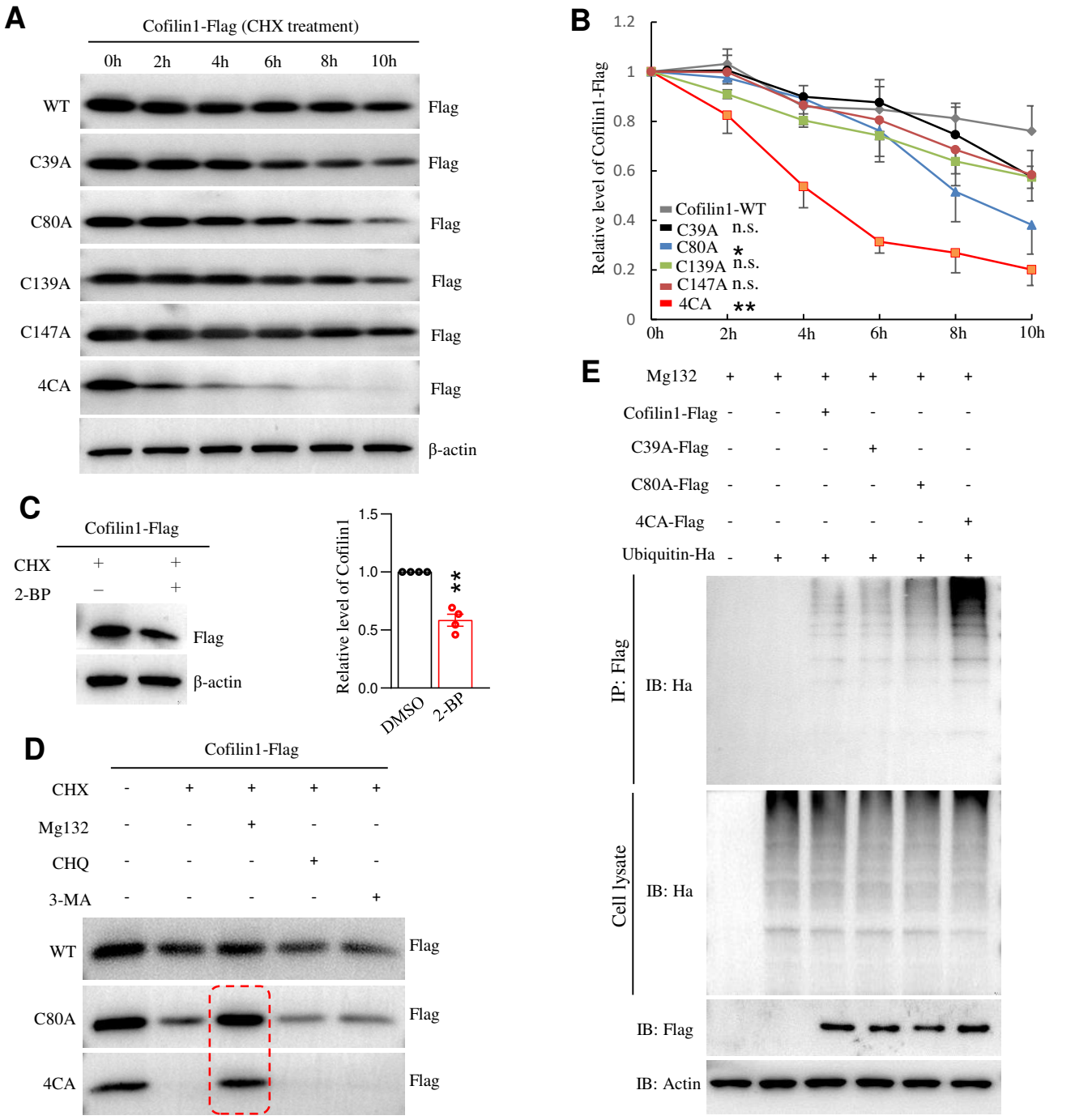

A
Cofilin1-Flag (CHX treatment)
0h 2h 4h 6h 8h 10h
WT
C39A
C80A
C139A
C147A
4CA
Flag
β-actin
B
Relative level of Cofilin1-Flag
Cofilin1-WT
C39A n.s.
C80A *
C139A n.s.
C147A n.s.
4CA **
0h 2h 4h 6h 8h 10h
C
Cofilin1-Flag
CHX + +
2-BP − +
Flag
β-actin
Relative level of Cofilin1
DMSO 2-BP
D
Cofilin1-Flag
CHX - + + + +
Mg132 - - + - -
CHQ - - - + -
3-MA - - - - +
WT
C80A
4CA
Flag
E
Mg132 + + + + + +
Cofilin1-Flag - - + - - -
C39A-Flag - - - + - -
C80A-Flag - - - - + -
4CA-Flag - - - - - +
Ubiquitin-Ha - + + + + +
IP: Flag
IB: Ha
Cell lysate
IB: Ha
IB: Flag
IB: Actin

Fig. 3

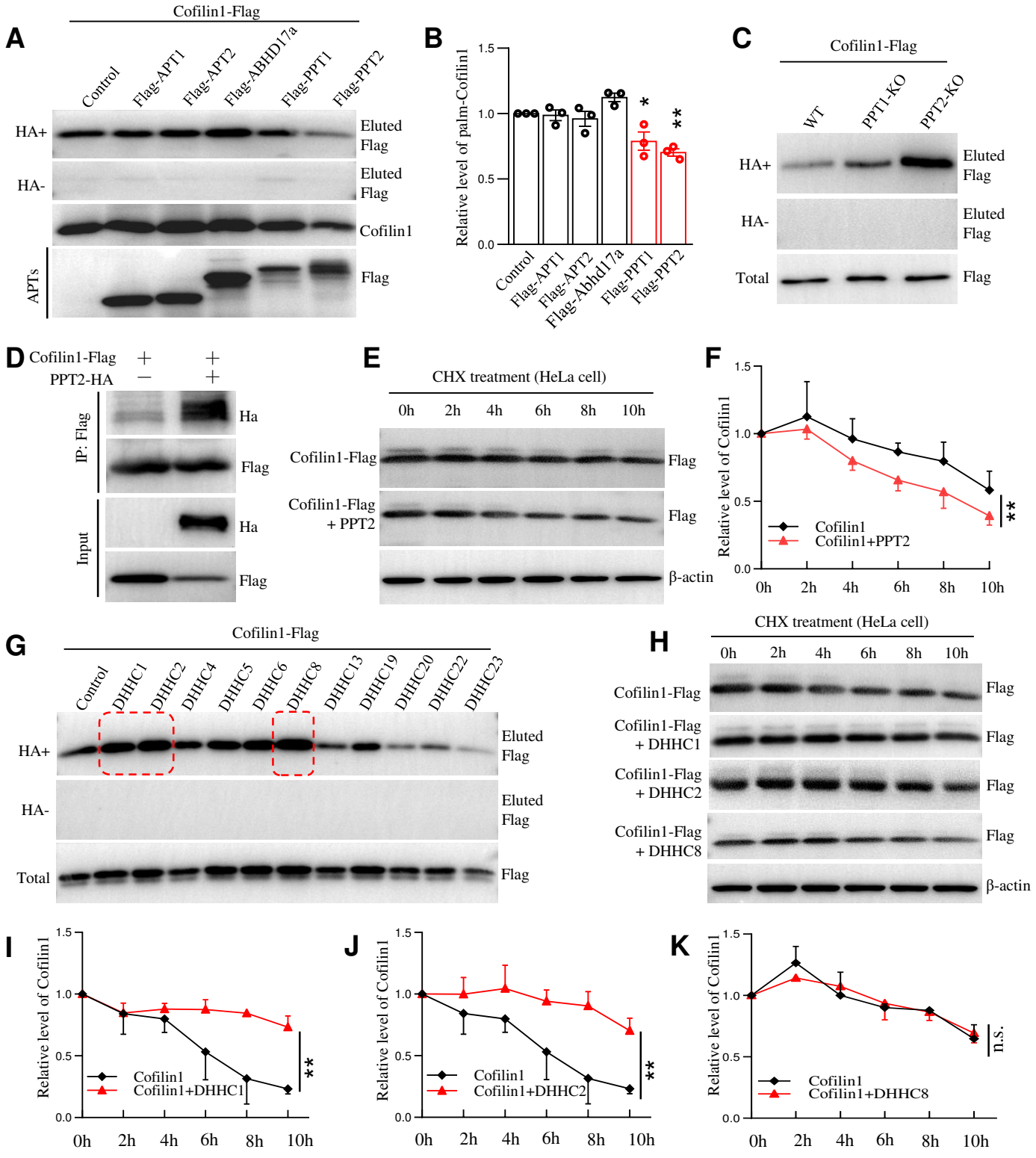

A
Cofilin1-Flag
Control
Flag-APT1
Flag-APT2
Flag-ABHD17a
Flag-PPT1
Flag-PPT2
HA+
HA-
APTs
Eluted Flag
Cofilin1
Flag
B
Relative level of palm-Cofilin1
C
Cofilin1-Flag
WT
PPT1-KO
PPT2-KO
Total
D
Cofilin1-Flag
PPT2-HA
IP: Flag
Input
Ha
E
CHX treatment (HeLa cell)
0h
2h
4h
6h
8h
10h
Cofilin1-Flag
Cofilin1-Flag + PPT2
β-actin
F
Relative level of Cofilin1
Cofilin1
Cofilin1+PPT2
G
DHHC1
DHHC2
DHHC4
DHHC5
DHHC6
DHHC8
DHHC13
DHHC19
DHHC20
DHHC22
DHHC23
H
Cofilin1-Flag + DHHC1
Cofilin1-Flag + DHHC2
Cofilin1-Flag + DHHC8
I
Cofilin1+DHHC1
J
Cofilin1+DHHC2
K
Cofilin1+DHHC8
n.s.

Fig. 4

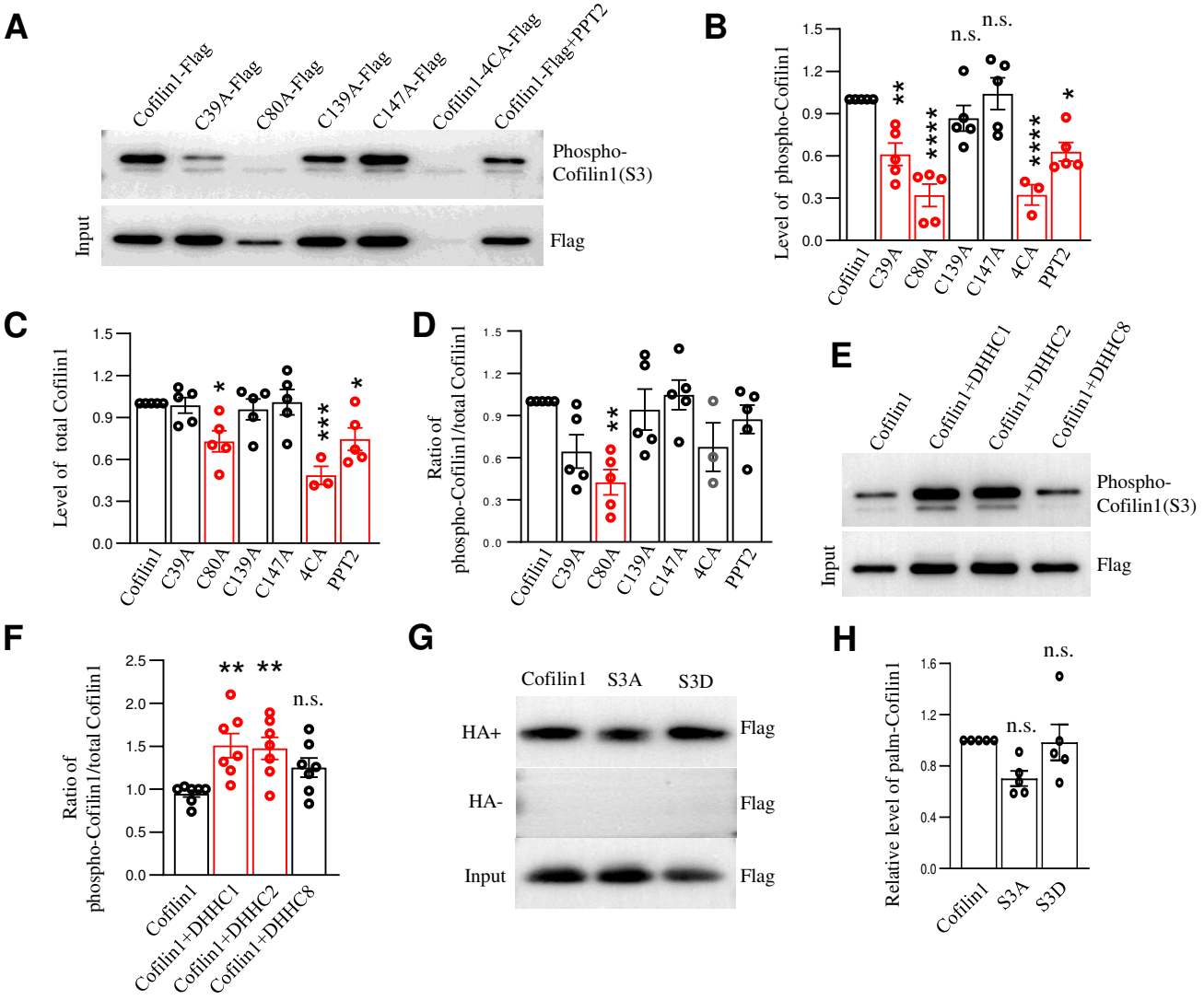

A
Cofilin1-Flag
C39A-Flag
C80A-Flag
C139A-Flag
C147A-Flag
Cofilin1-4CA-Flag
Cofilin1-Flag+PPT2
Phospho-Cofilin1(S3)
Input
Flag
B
Level of phospho-Cofilin1
n.s.
n.s.
Cofilin1
C39A
C80A
C139A
C147A
4CA
PPT2
C
Level of total Cofilin1
D
Ratio of phospho-Cofilin1/total Cofilin1
E
Cofilin1
Cofilin1+DHHC1
Cofilin1+DHHC2
Cofilin1+DHHC8
Phospho-Cofilin1(S3)
Input
Flag
F
Ratio of phospho-Cofilin1/total Cofilin1
n.s.
G
Cofilin1
S3A
S3D
HA+
HA-
Input
Flag
H
Relative level of palm-Cofilin1
n.s.
n.s.
S3A
S3D

Fig. 5

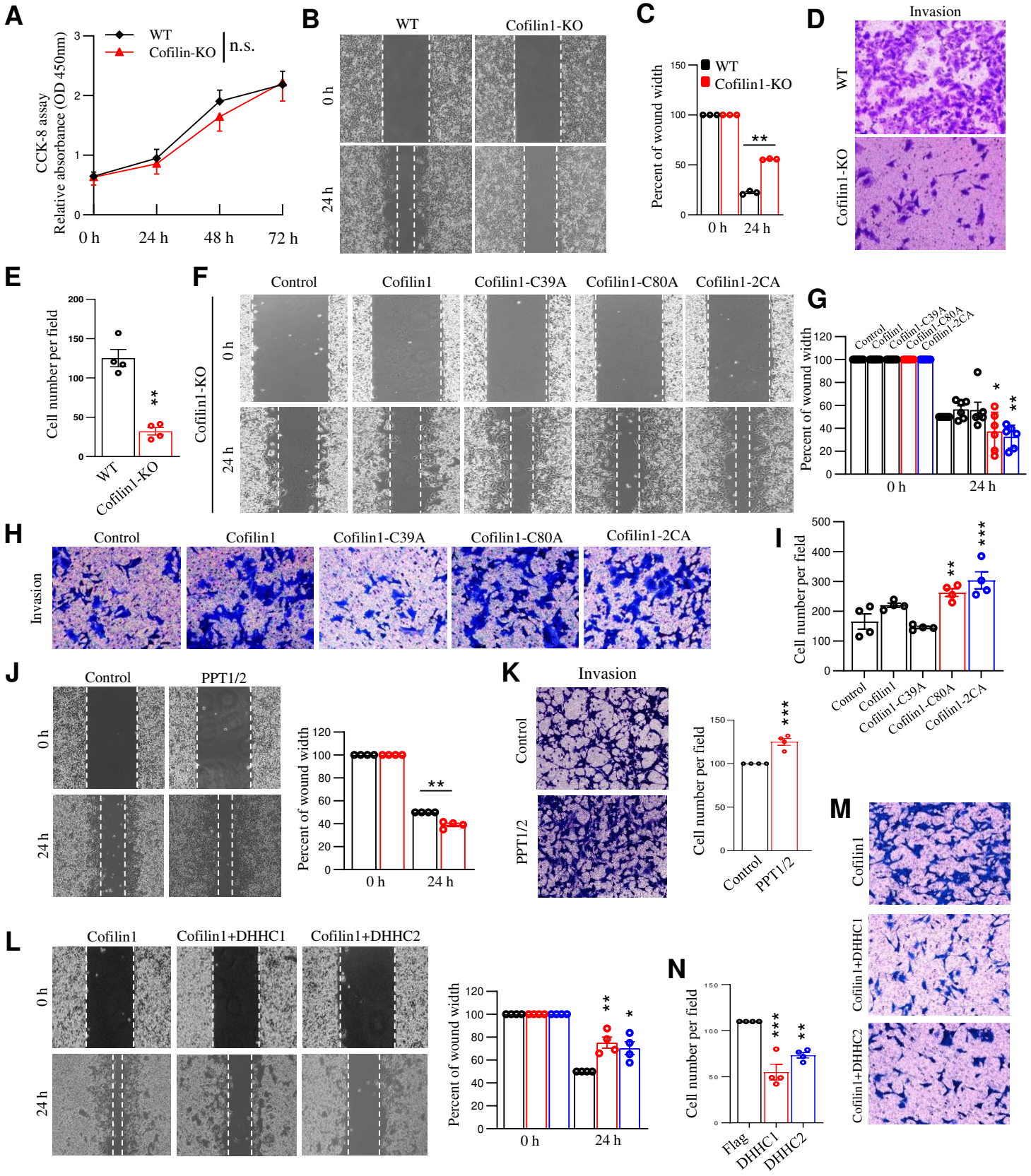

A
WT
Cofilin-KO
n.s.
CCK-8 assay
Relative absorbance (OD 450nm)
0 h
24 h
48 h
72 h
B
WT
Cofilin1-KO
0 h
24 h
C
WT
Cofilin1-KO
Percent of wound width
**
0 h
24 h
D
Invasion
WT
Cofilin1-KO
E
Cell number per field
**
WT
Cofilin1-KO
F
Control
Cofilin1
Cofilin1-C39A
Cofilin1-C80A
Cofilin1-2CA
Cofilin1-KO
0 h
24 h
G
Control
Cofilin1
Cofilin1-C39A
Cofilin1-C80A
Cofilin1-2CA
Percent of wound width
*
**
0 h
24 h
H
Control
Cofilin1
Cofilin1-C39A
Cofilin1-C80A
Cofilin1-2CA
Invasion
I
Cell number per field
**
***
Control
Cofilin1
Cofilin1-C39A
Cofilin1-C80A
Cofilin1-2CA
J
Control
PPT1/2
0 h
24 h
Percent of wound width
**
0 h
24 h
K
Invasion
Control
PPT1/2
Cell number per field
***
Control
PPT1/2
M
Cofilin1
Cofilin1+DHHC1
Cofilin1+DHHC2
L
Cofilin1
Cofilin1+DHHC1
Cofilin1+DHHC2
0 h
24 h
Percent of wound width
**
*
0 h
24 h
N
Cell number per field
***
**
Flag
DHHC1
DHHC2

Fig. 6

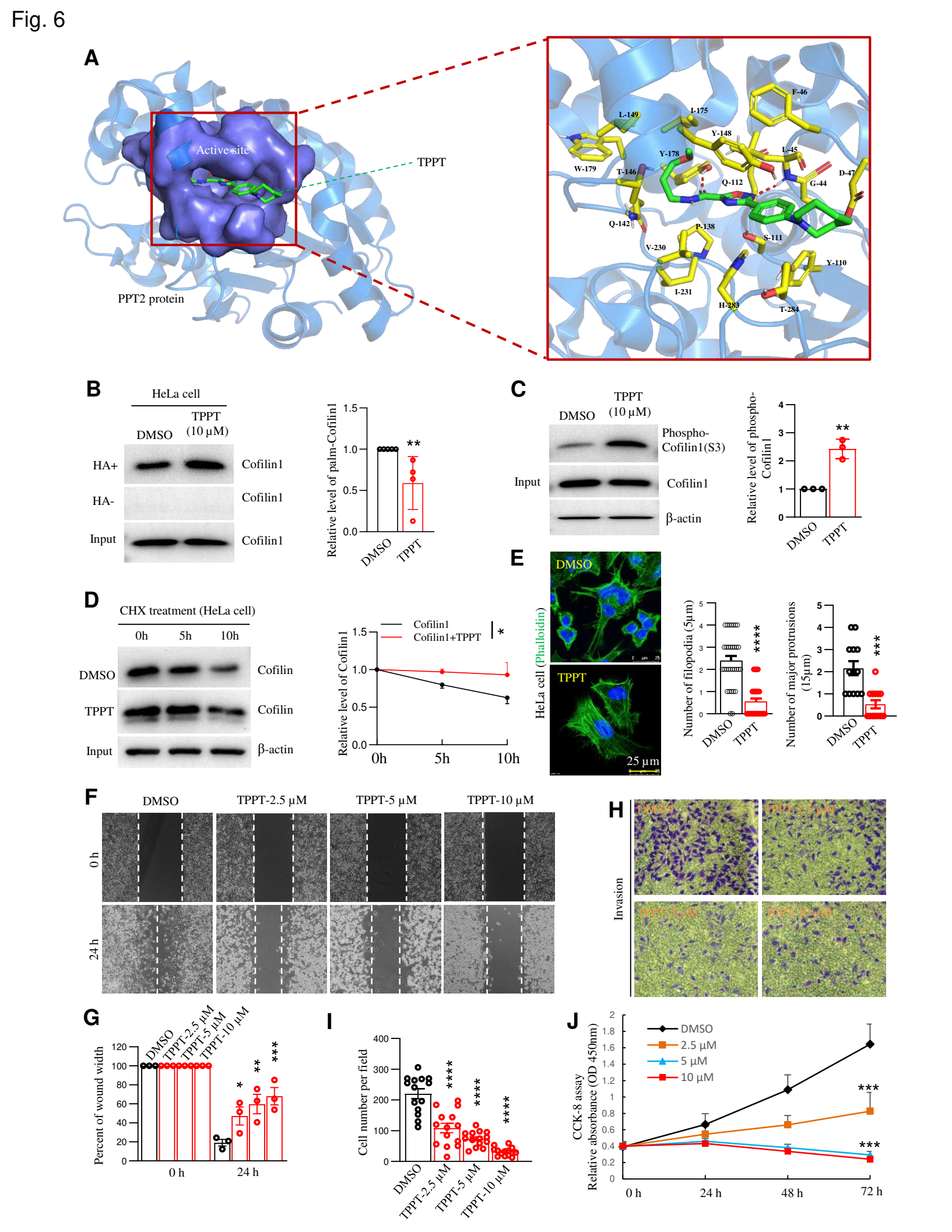

A
Active site
TPPT
PPT2 protein
F-46
L-149
I-175
Y-148
Y-178
L-45
W-179
T-146
Q-112
D-47
G-44
Q-142
P-138
S-111
V-230
Y-110
I-231
H-283
T-284
B
HeLa cell
DMSO
TPPT (10 μM)
HA+
HA-
Input
Cofilin1
Relative level of palm-Cofilin1
C
Phospho-Cofilin1(S3)
β-actin
Relative level of phospho-Cofilin1
D
CHX treatment (HeLa cell)
0h
5h
10h
Cofilin
Cofilin1+TPPT
Relative level of Cofilin1
E
HeLa cell (Phalloidin)
25 μm
Number of filopodia (5μm)
Number of major protrusions (15μm)
F
TPPT-2.5 μM
TPPT-5 μM
TPPT-10 μM
0 h
24 h
H
Invasion
G
Percent of wound width
I
Cell number per field
J
CCK-8 assay
Relative absorbance (OD 450nm)
2.5 μM
5 μM
10 μM
48 h
72 h

Fig. 7

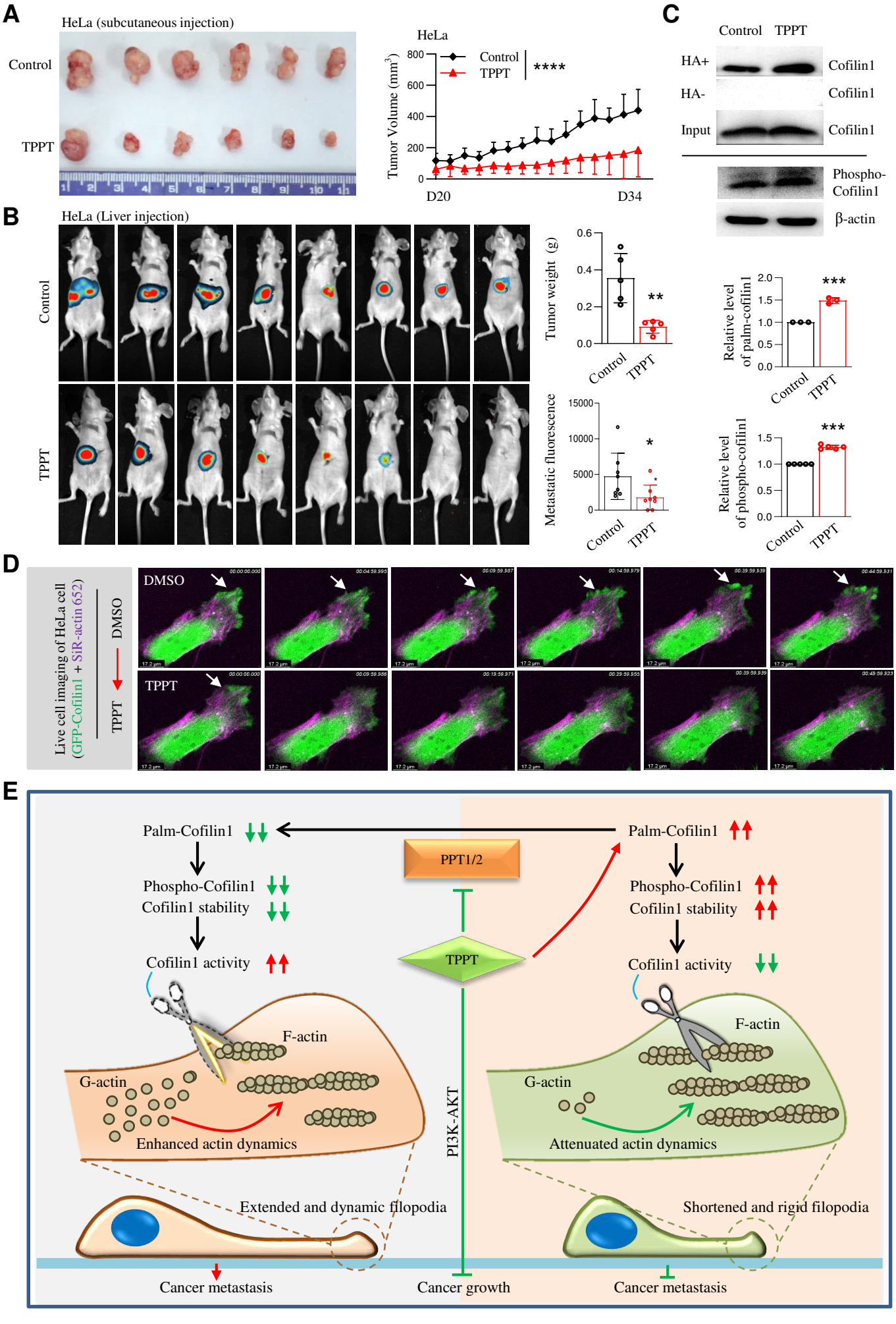

A
HeLa (subcutaneous injection)
Control
TPPT
HeLa
Control
TPPT
****
Tumor Volume (mm3)
800
600
400
200
0
D20
D34
B
HeLa (Liver injection)
Control
TPPT
Tumor weight (g)
0.6
0.4
0.2
0.0
**
Control
TPPT
Metastatic fluorescence
15000
10000
5000
0
*
Control
TPPT
C
Control
TPPT
HA+
Cofilin1
HA-
Cofilin1
Input
Cofilin1
Phospho-Cofilin1
β-actin
Relative level of palm-cofilin1
2.0
1.5
1.0
0.5
0.0
***
Control
TPPT
Relative level of phospho-cofilin1
1.5
1.0
0.5
0.0
***
Control
TPPT
D
Live cell imaging of HeLa cell (GFP-Cofilin1 + SiR-actin 652)
DMSO
TPPT
DMSO
TPPT
E
Palm-Cofilin1
Phospho-Cofilin1
Cofilin1 stability
Cofilin1 activity
PPT1/2
TPPT
Palm-Cofilin1
Phospho-Cofilin1
Cofilin1 stability
Cofilin1 activity
F-actin
G-actin
Enhanced actin dynamics
F-actin
G-actin
Attenuated actin dynamics
PI3K-AKT
Extended and dynamic filopodia
Shortened and rigid filopodia
Cancer metastasis
Cancer growth
Cancer metastasis

Fig. S1

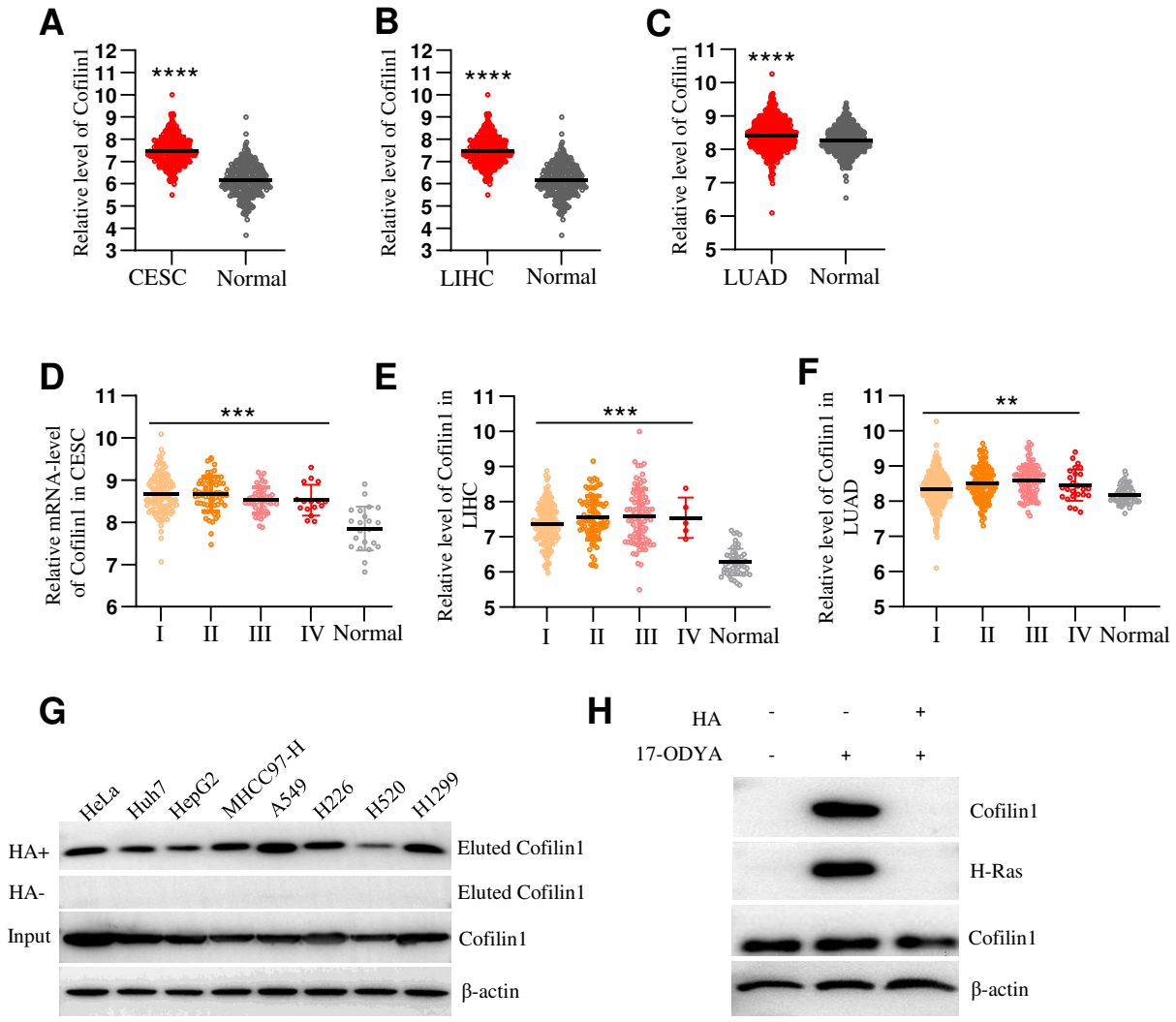

A
B
C
Relative level of Cofilin1
****
CESC
Normal
LIHC
LUAD
D
E
F
Relative mRNA-level of Cofilin1 in CESC
Relative level of Cofilin1 in LIHC
Relative level of Cofilin1 in LUAD
***
**
I
II
III
IV
Normal
G
HeLa
Huh7
HepG2
MHCC97-H
A549
H226
H520
H1299
HA+
HA-
Input
Eluted Cofilin1
Cofilin1
β-actin
H
HA
17-ODYA
H-Ras

Fig. S2

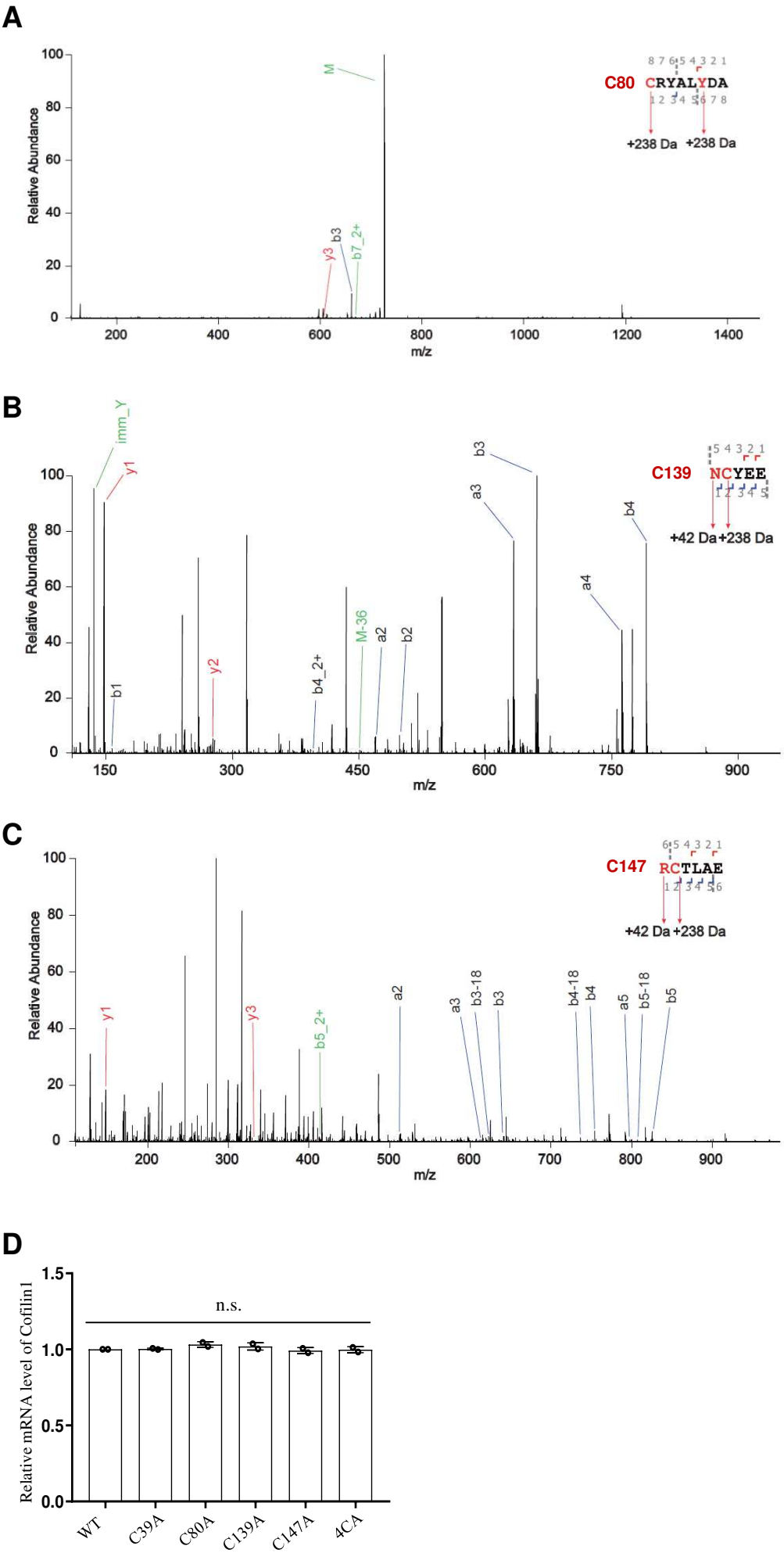
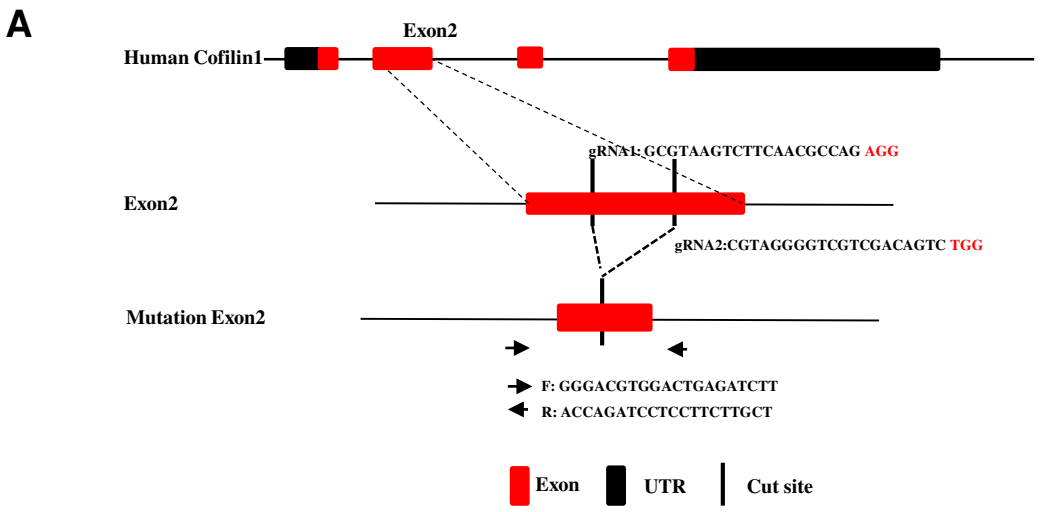
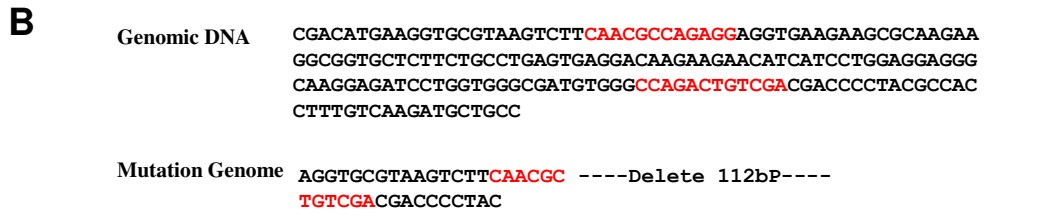
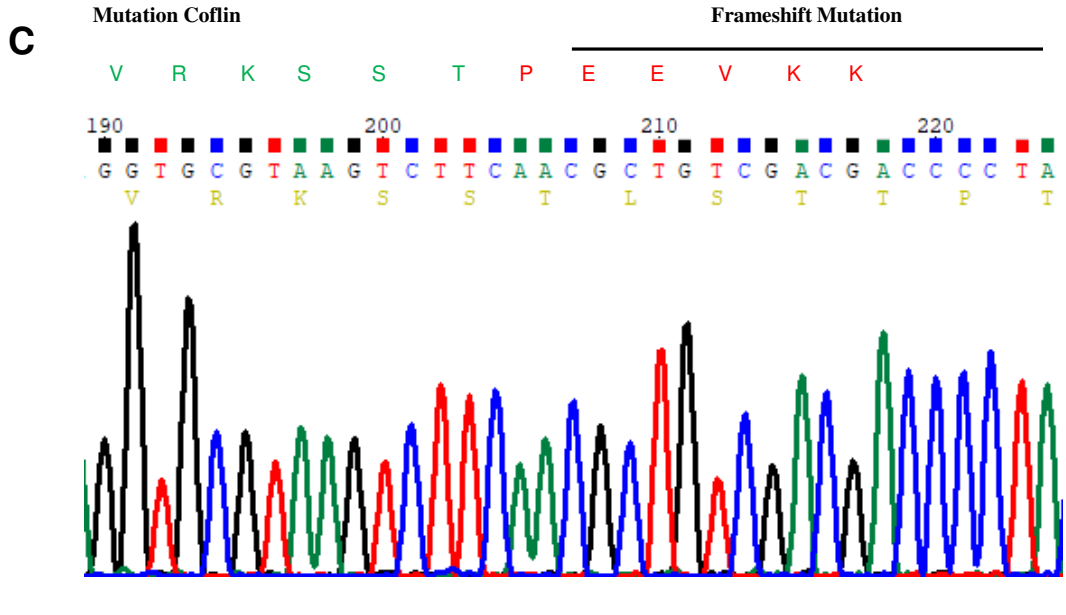
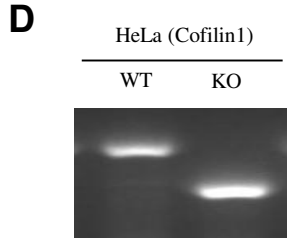

A
Relative Abundance
m/z
M
y3
b3
b7_2+
C80 CRYALYDA
+238 Da +238 Da
B
Relative Abundance
m/z
imm_Y
y1
y2
b1
b4_2+
M-36
a2
b2
a3
b3
a4
b4
C139 NCYEE
+42 Da +238 Da
C
Relative Abundance
m/z
y1
y3
b5_2+
a2
a3
b3-18
b3
b4-18
b4
a5
b5-18
b5
C147 RCTLAE
+42 Da +238 Da
D
Relative mRNA level of Cofilin1
n.s.
WT
C39A
C80A
C139A
C147A
4CA

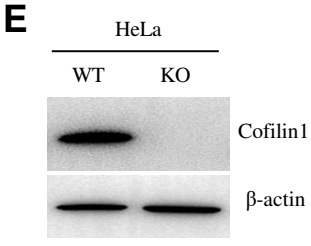
Fig. S3


A
Exon2
Human Cofilin1
gRNA1:GCGTAAGTCTTCAACGCCAG AGG
Exon2
gRNA2:CGTAGGGGTCGTCGACAGTC TGG
Mutation Exon2
F: GGGACGTGGACTGAGATCTT
R: ACCAGATCCTCCTTCTTGCT
Exon
UTR
Cut site


B
Genomic DNA
CGACATGAAGGTGCGTAAGTCTTCAACGCCAGAGGAGGTGAAGAAGCGCAAGAA
GGCGGTGCTCTTCTGCCTGAGTGAGGACAAGAAGAACATCATCCTGGAGGAGGG
CAAGGAGATCCTGGTGGGCGATGTGGGCCAGACTGTCGACGACCCCTACGCCAC
CTTTGTCAAGATGCTGCC
Mutation Genome
AGGTGCGTAAGTCTTCAACGC ----Delete 112bP----
TGTCGACGACCCCTAC


C
Mutation Coflin
Frameshift Mutation
V R K S S T P E E V K K
190 200 210 220
G G T G C G T A A G T C T T C A A C G C C T G T C G A C G A C C C C T A
V R K S S T L S T T P T


D
HeLa (Cofilin1)
WT
KO


E
HeLa
WT
KO
Cofilin1
β-actin

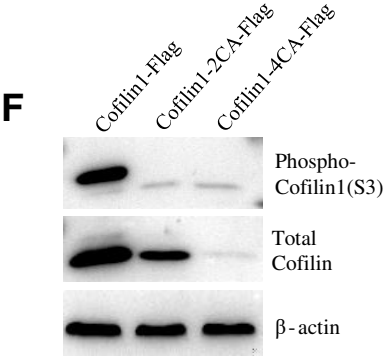
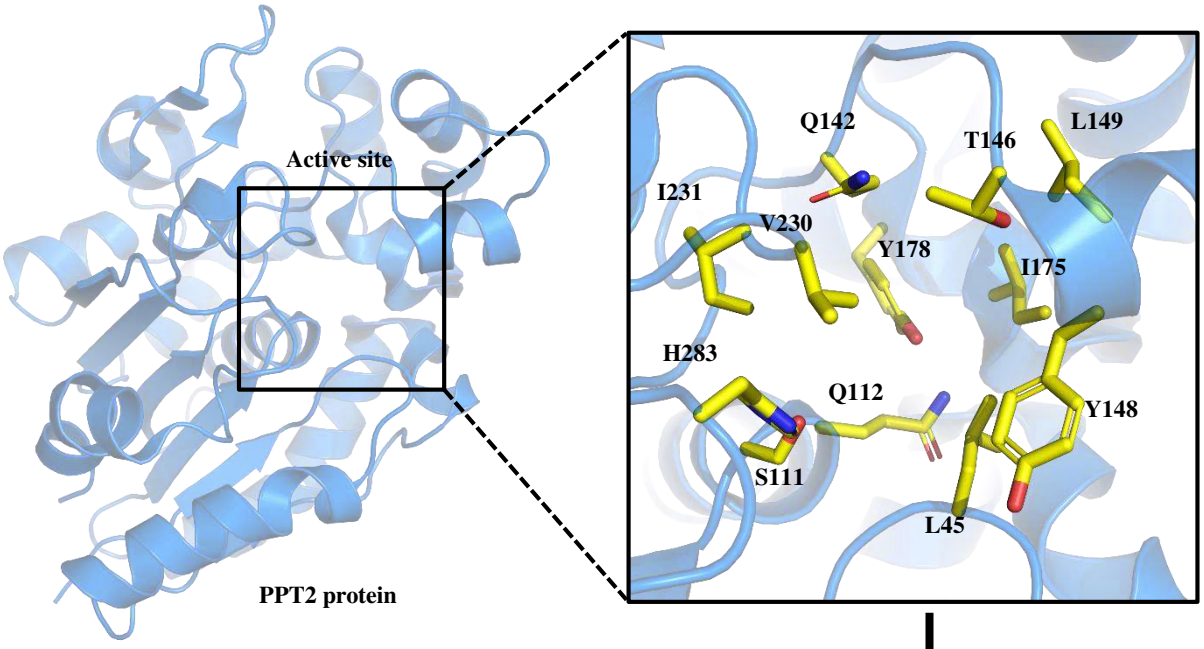

F
Cofilin1-Flag
Cofilin1-2CA-Flag
Cofilin1-4CA-Flag
Phospho-Cofilin1(S3)
Total Cofilin
β-actin

Fig. S4



ChemDiv
1,600,000

Lipinski`s rule of five

1,060,000

Fast docking

10,600

Normative docking

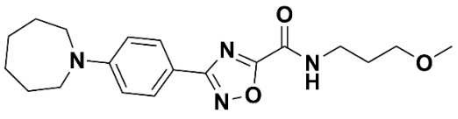
500

Clustering & Selection

34 hits
selected

Validation in HeLa cells by RAC assay
for the regulation of palm-Cofilin1

1 hit
selected



L471-1746 (TPPT)

Fig. S5

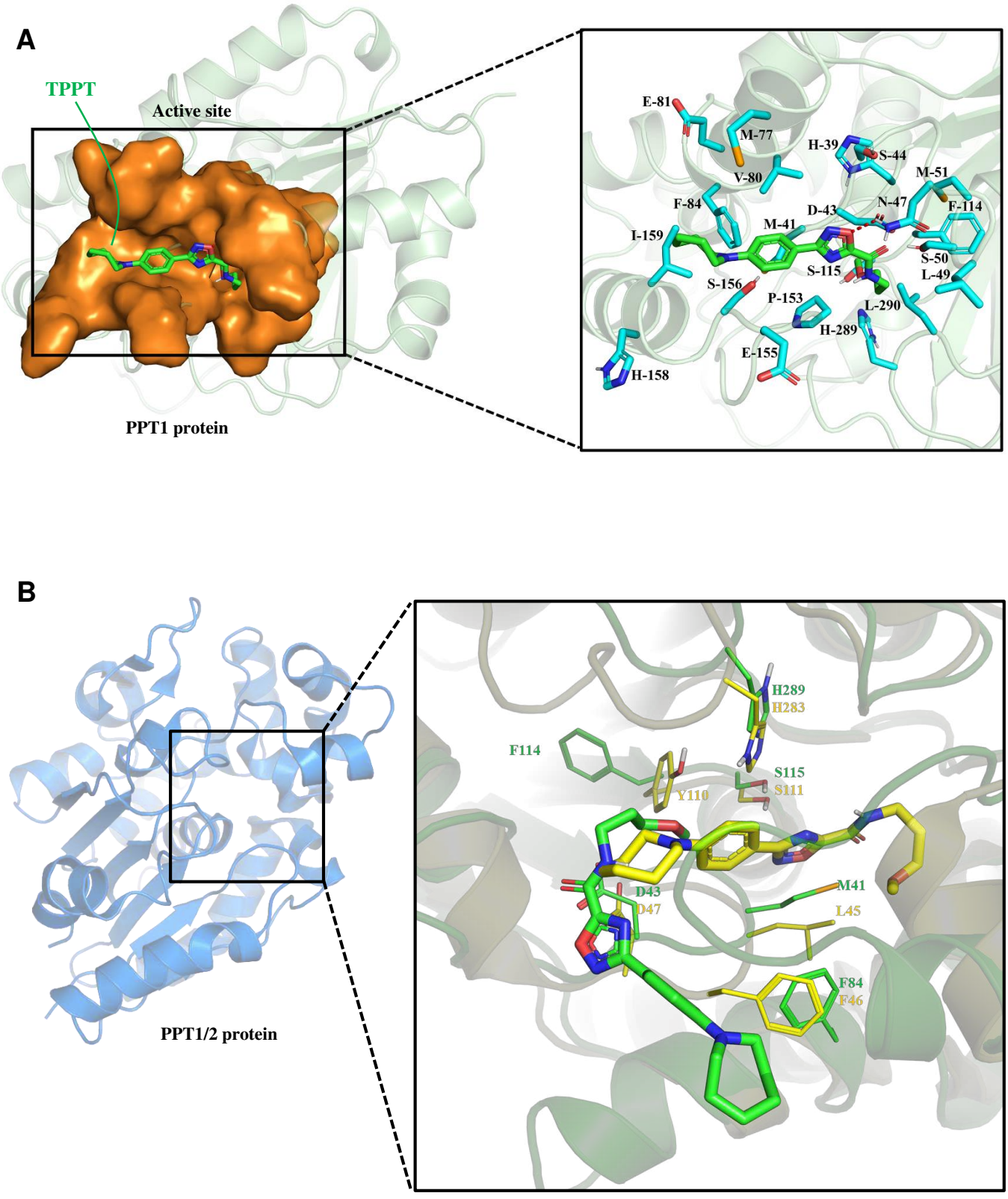

A
TPPT
Active site
PPT1 protein
E-81
M-77
V-80
H-39
S-44
M-51
F-84
D-43
N-47
F-114
M-41
I-159
S-50
L-49
S-115
S-156
P-153
L-290
H-289
E-155
H-158
B
PPT1/2 protein
H289
H283
F114
S115
S111
Y110
M41
D43
D47
L45
F84
F46

Fig. S6

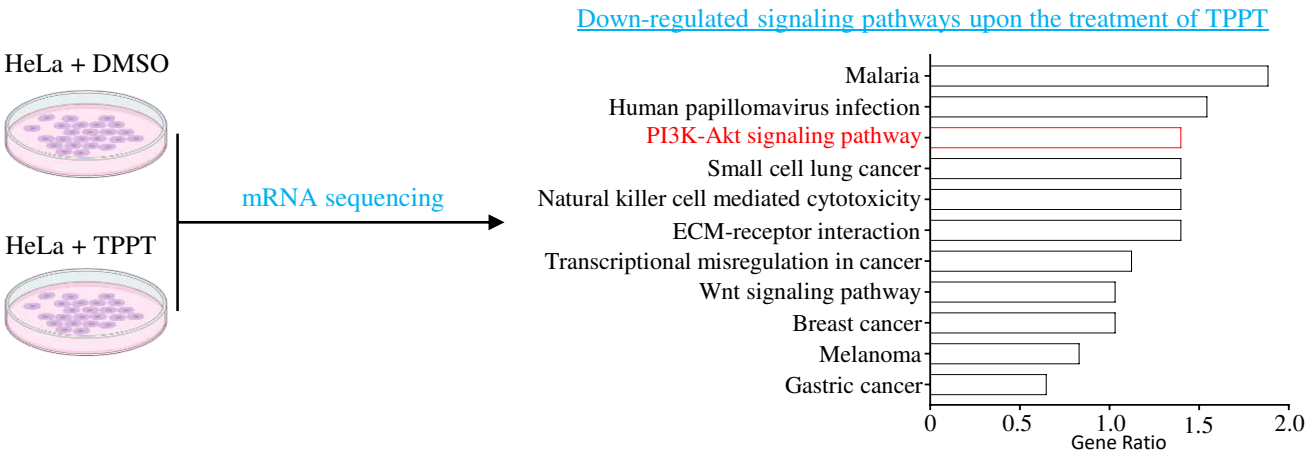

HeLa + DMSO
HeLa + TPPT
mRNA sequencing
Down-regulated signaling pathways upon the treatment of TPPT
Malaria
Human papillomavirus infection
PI3K-Akt signaling pathway
Small cell lung cancer
Natural killer cell mediated cytotoxicity
ECM-receptor interaction
Transcriptional misregulation in cancer
Wnt signaling pathway
Breast cancer
Melanoma
Gastric cancer
0
0.5
1.0
1.5
2.0
Gene Ratio

Fig. S7

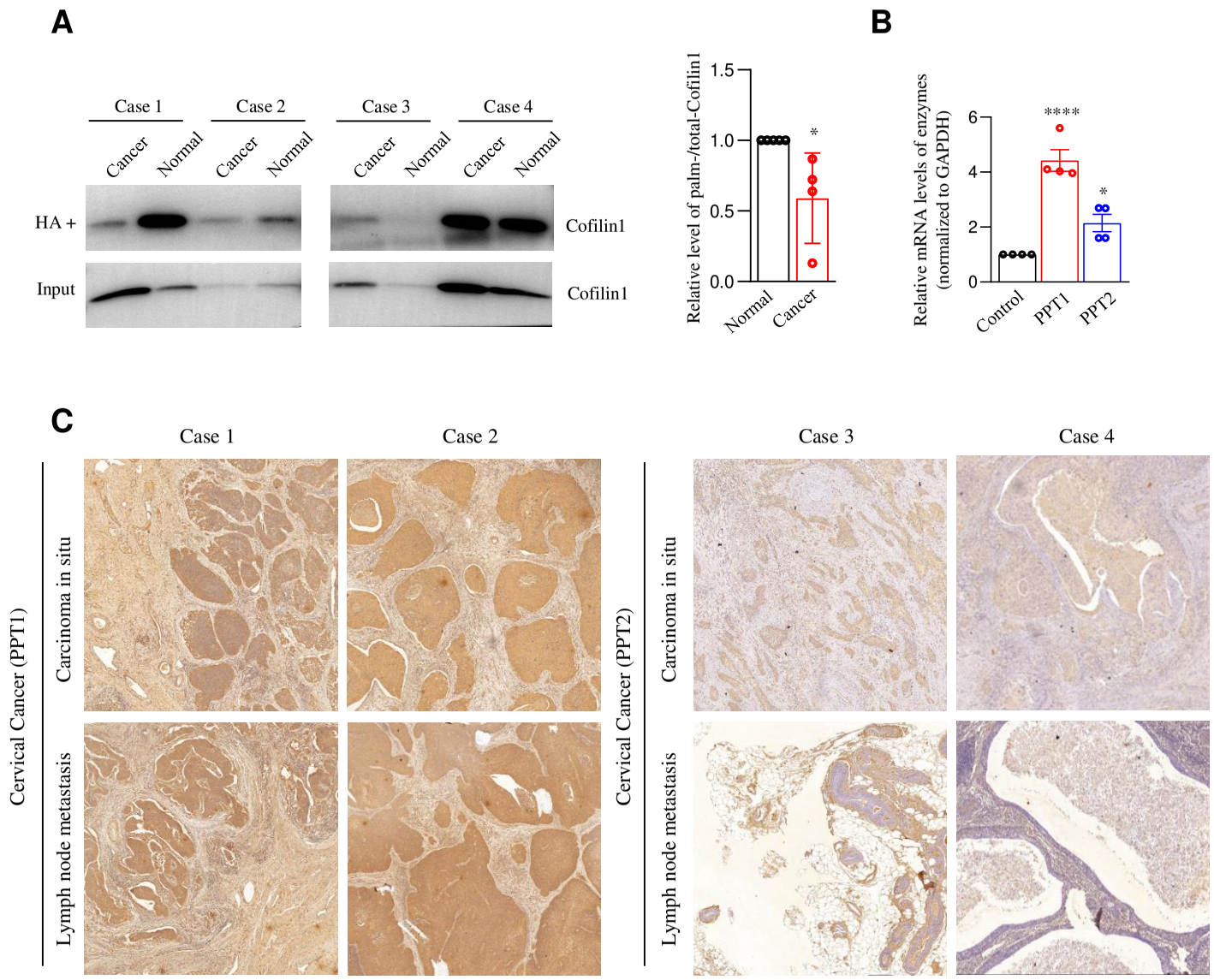

A
Case 1
Case 2
Case 3
Case 4
Cancer
Normal
HA +
Input
Cofilin1
Cofilin1
Relative level of palm-/total-Cofilin1
1.5
1.0
0.5
0.0
*
Normal
Cancer
B
Relative mRNA levels of enzymes (normalized to GAPDH)
6
4
2
0
****
*
Control
PPT1
PPT2
C
Case 1
Case 2
Case 3
Case 4
Cervical Cancer (PPT1)
Carcinoma in situ
Lymph node metastasis
Cervical Cancer (PPT2)
Carcinoma in situ
Lymph node metastasis

Fig. S8

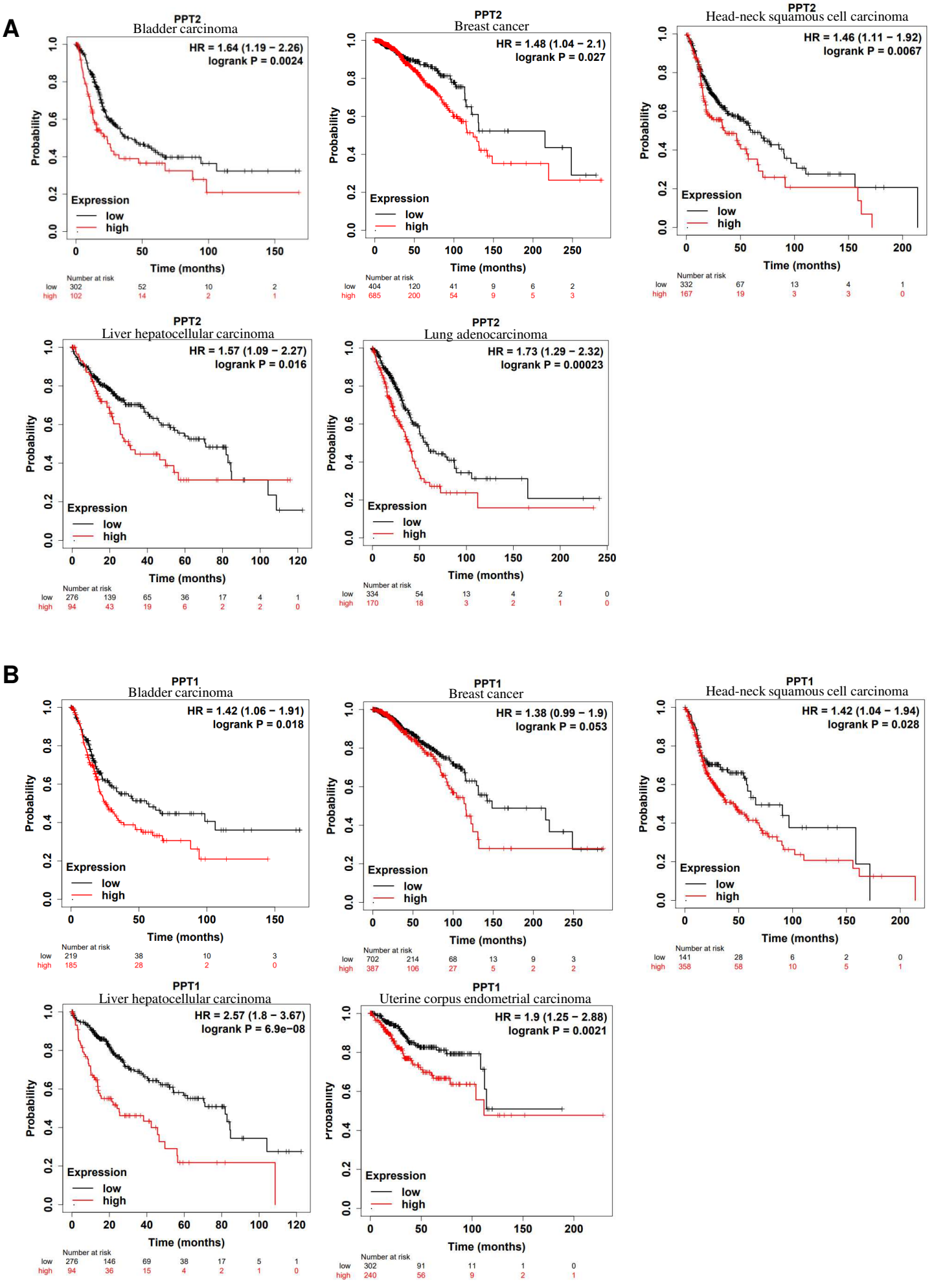

A
PPT2
Bladder carcinoma
HR = 1.64 (1.19 − 2.26)
logrank P = 0.0024
PPT2
Breast cancer
HR = 1.48 (1.04 − 2.1)
logrank P = 0.027
PPT2
Head-neck squamous cell carcinoma
HR = 1.46 (1.11 − 1.92)
logrank P = 0.0067
PPT2
Liver hepatocellular carcinoma
HR = 1.57 (1.09 − 2.27)
logrank P = 0.016
PPT2
Lung adenocarcinoma
HR = 1.73 (1.29 − 2.32)
logrank P = 0.00023
B
PPT1
Bladder carcinoma
HR = 1.42 (1.06 − 1.91)
logrank P = 0.018
PPT1
Breast cancer
HR = 1.38 (0.99 − 1.9)
logrank P = 0.053
PPT1
Head-neck squamous cell carcinoma
HR = 1.42 (1.04 − 1.94)
logrank P = 0.028
PPT1
Liver hepatocellular carcinoma
HR = 2.57 (1.8 − 3.67)
logrank P = 6.9e−08
PPT1
Uterine corpus endometrial carcinoma
HR = 1.9 (1.25 − 2.88)
logrank P = 0.0021
Probability
Expression
low
high
Time (months)
Number at risk

Fig. S9

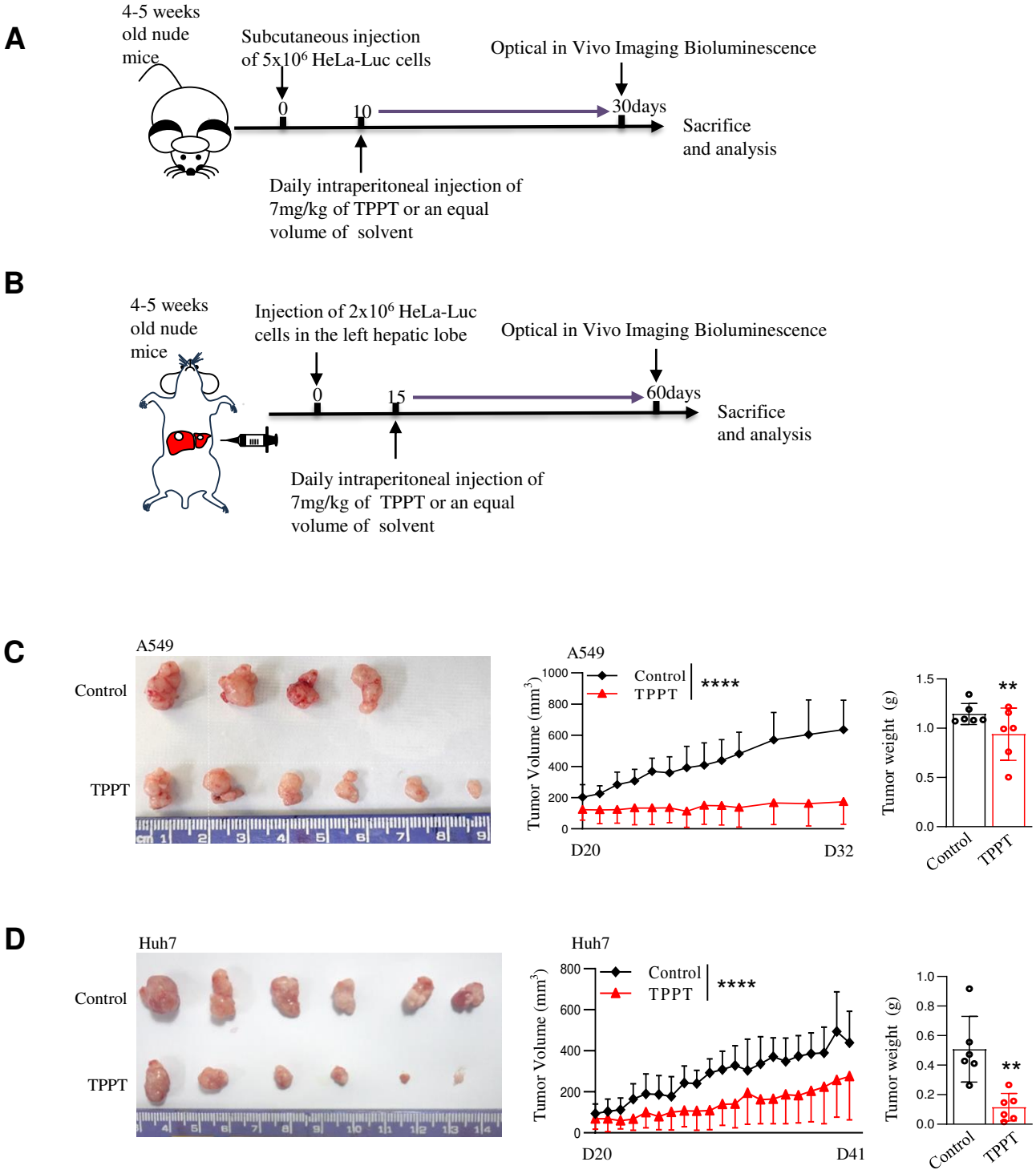

A
4-5 weeks old nude mice
Subcutaneous injection of 5x10⁶ HeLa-Luc cells
Optical in Vivo Imaging Bioluminescence
0
10
30days
Sacrifice and analysis
Daily intraperitoneal injection of 7mg/kg of TPPT or an equal volume of solvent
B
4-5 weeks old nude mice
Injection of 2x10⁶ HeLa-Luc cells in the left hepatic lobe
Optical in Vivo Imaging Bioluminescence
0
15
60days
Sacrifice and analysis
Daily intraperitoneal injection of 7mg/kg of TPPT or an equal volume of solvent
C
A549
Control
TPPT
A549
Control
TPPT
****
Tumor Volume (mm³)
D20
D32
Tumor weight (g)
**
Control
TPPT
D
Huh7
Control
TPPT
Huh7
Control
TPPT
****
Tumor Volume (mm³)
D20
D41
Tumor weight (g)
**
Control
TPPT

Fig. S10

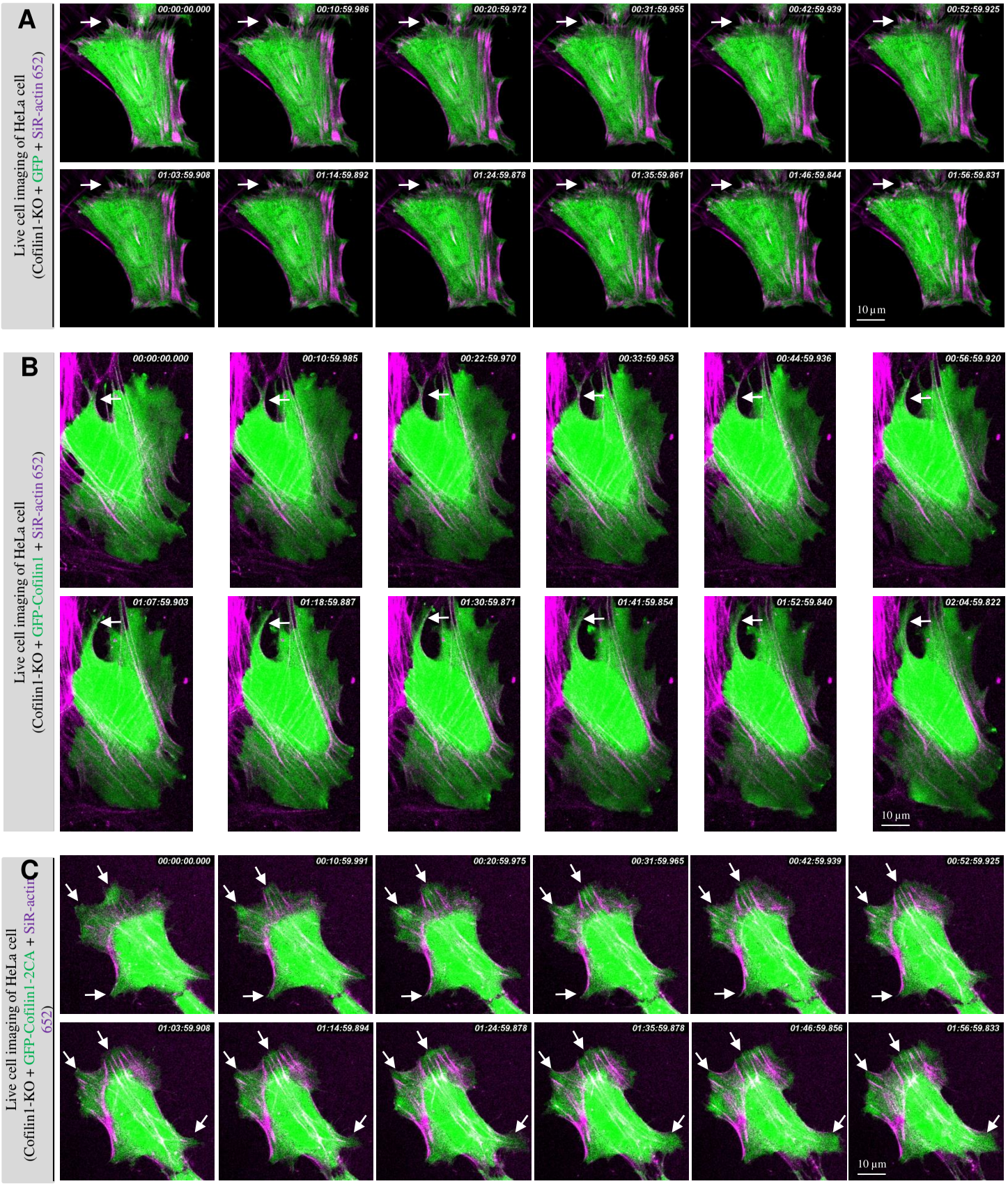
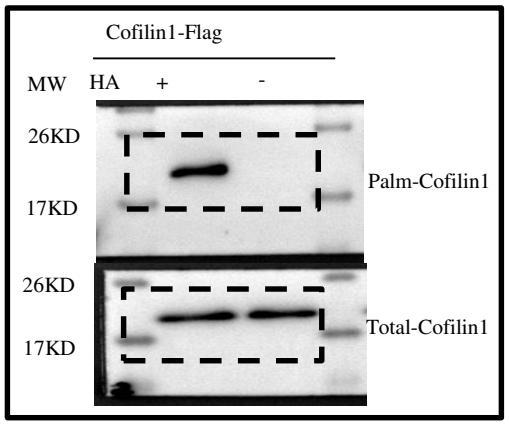
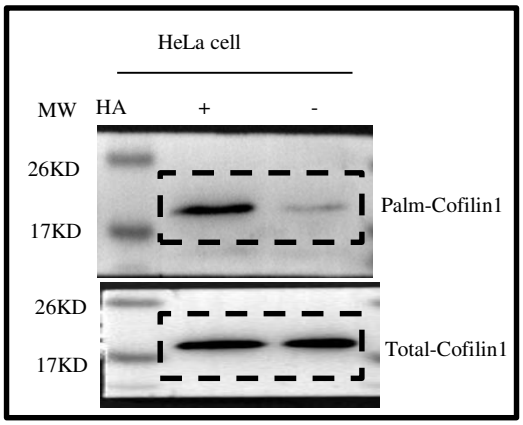

A
Live cell imaging of HeLa cell
(Cofilin1-KO + GFP + SiR-actin 652)
00:00:00.000
00:10:59.986
00:20:59.972
00:31:59.955
00:42:59.939
00:52:59.925
01:03:59.908
01:14:59.892
01:24:59.878
01:35:59.861
01:46:59.844
01:56:59.831
10 µm
B
Live cell imaging of HeLa cell
(Cofilin1-KO + GFP-Cofilin1 + SiR-actin 652)
00:00:00.000
00:10:59.985
00:22:59.970
00:33:59.953
00:44:59.936
00:56:59.920
01:07:59.903
01:18:59.887
01:30:59.871
01:41:59.854
01:52:59.840
02:04:59.822
10 µm
C
Live cell imaging of HeLa cell
(Cofilin1-KO + GFP-Cofilin1-2CA + SiR-actin 652)
00:00:00.000
00:10:59.991
00:20:59.975
00:31:59.965
00:42:59.939
00:52:59.925
01:03:59.908
01:14:59.894
01:24:59.878
01:35:59.878
01:46:59.856
01:56:59.833
10 µm

Fig. S11

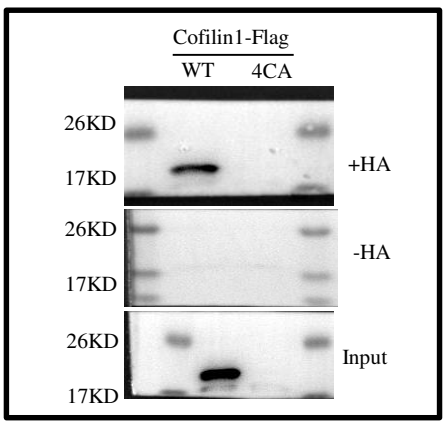
Uncropped blot of Fig.1C



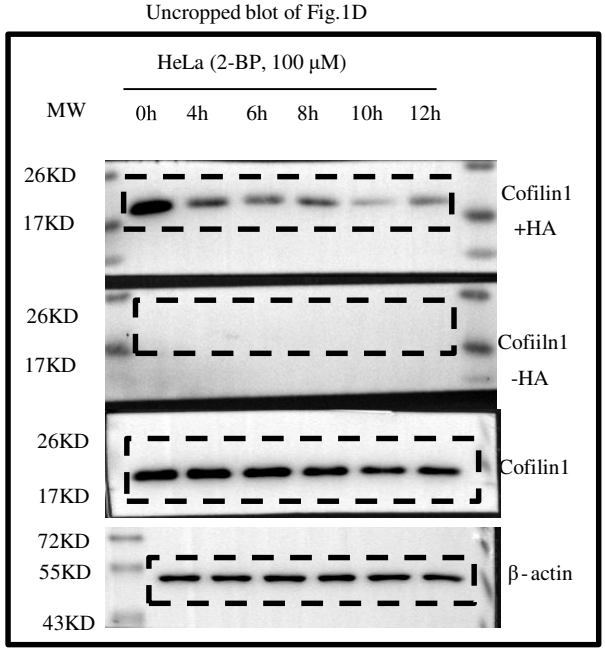
Uncropped blot of Fig.1C



Uncropped blot of Fig.1I



Uncropped blot of Fig.1D



Uncropped blot of Fig.1G

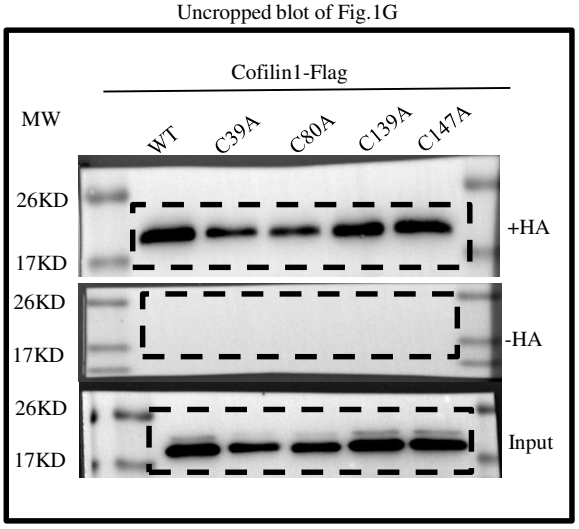
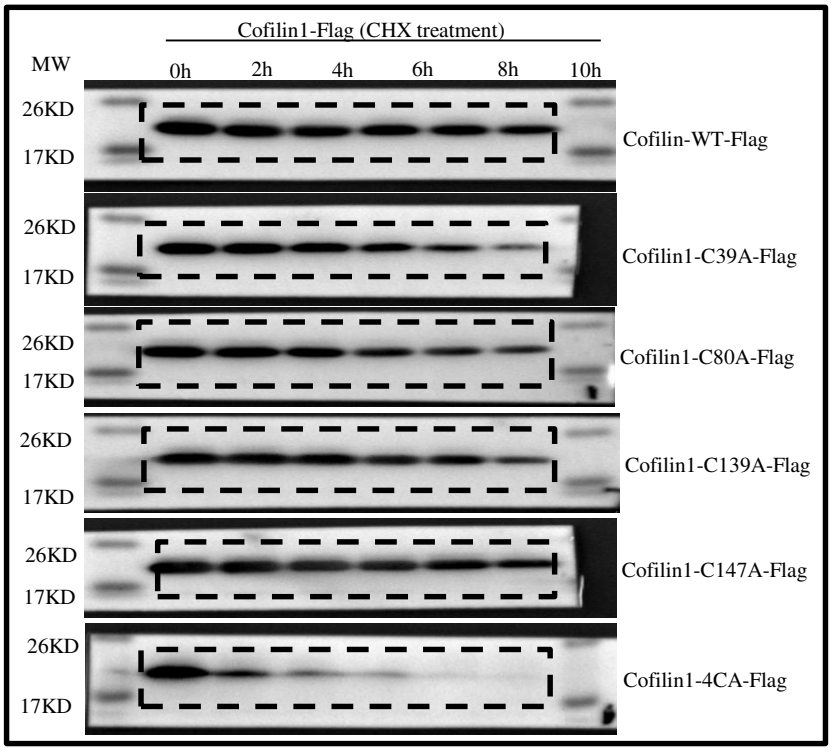
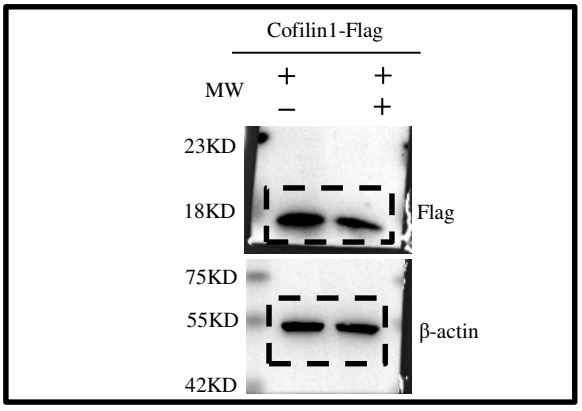


Fig. S12

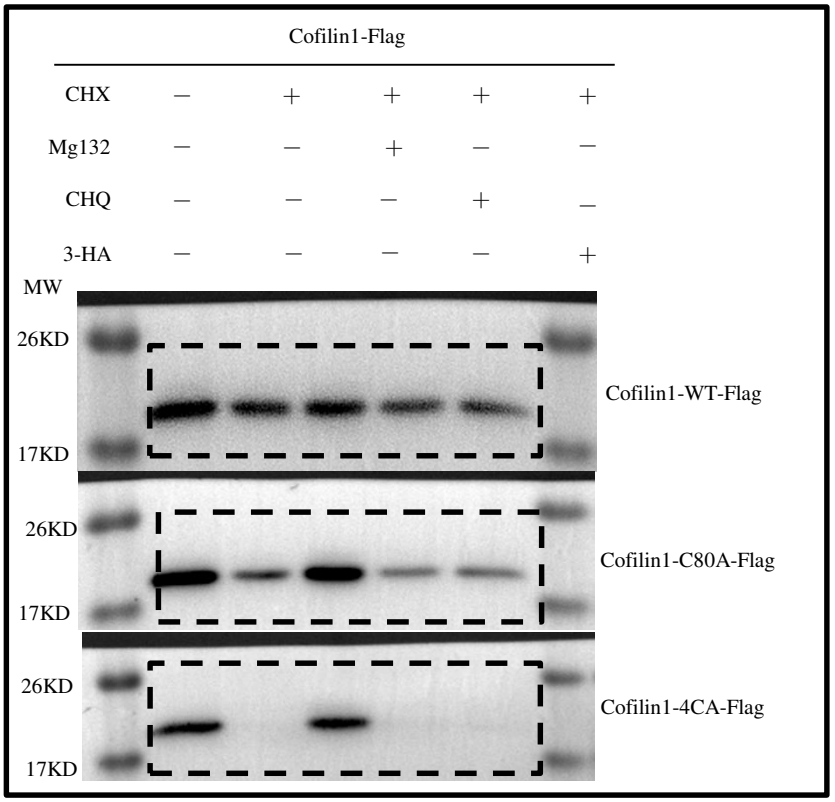
Uncropped blot of Fig.2A



Uncropped blot of Fig.2C



Uncropped blot of Fig.2D



Uncropped blot of Fig.2E

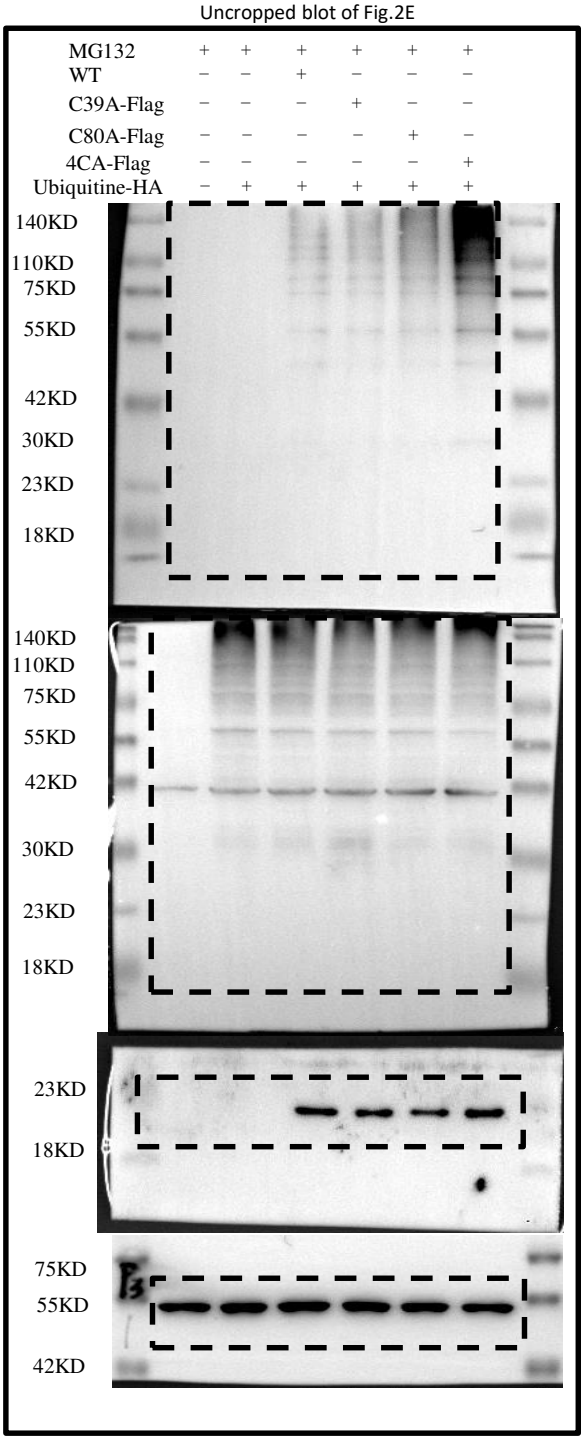
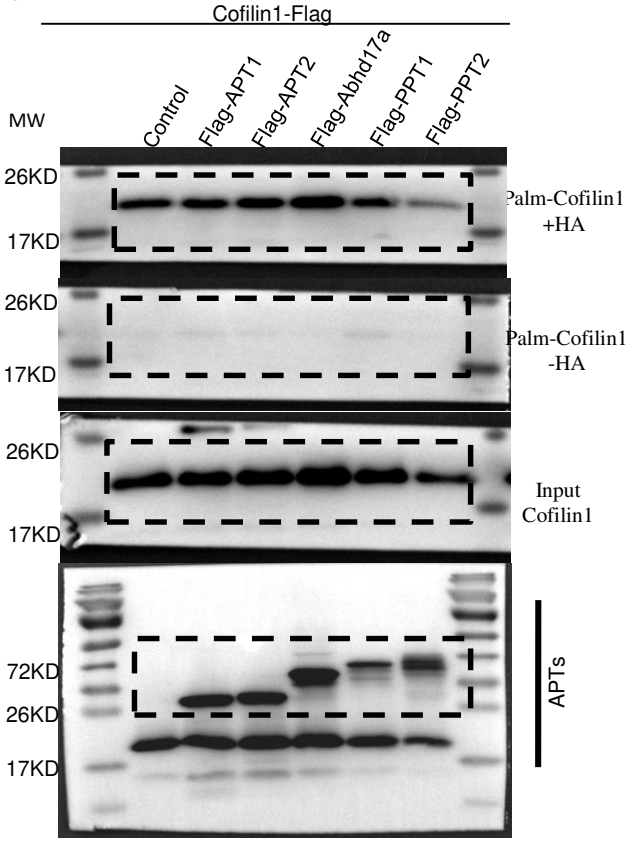
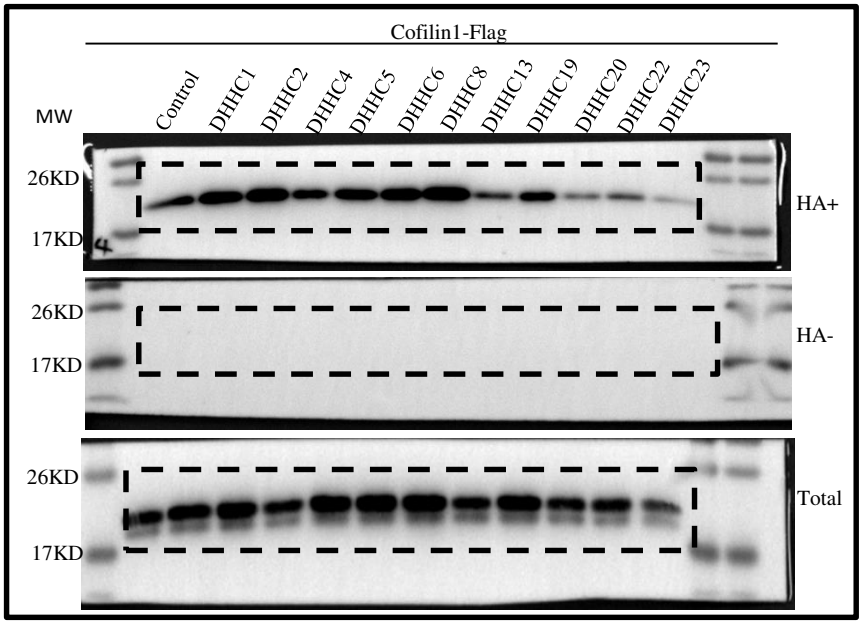


Fig. S13

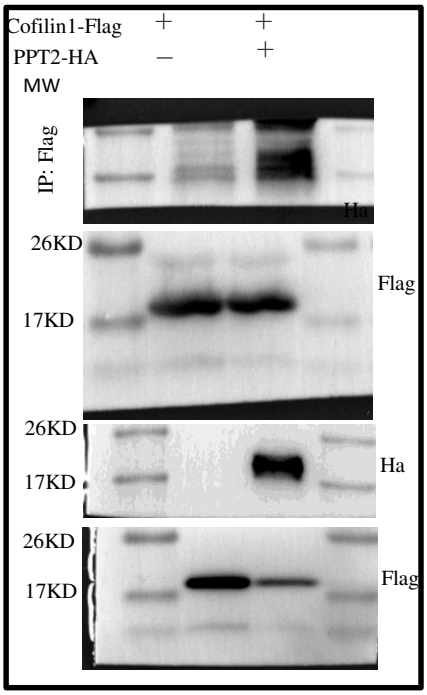
Uncropped blot of Fig.3A



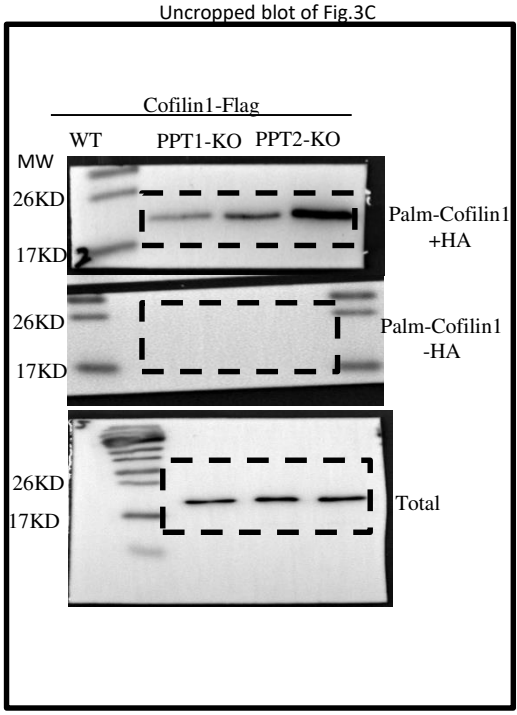
Uncropped blot of Fig.3G



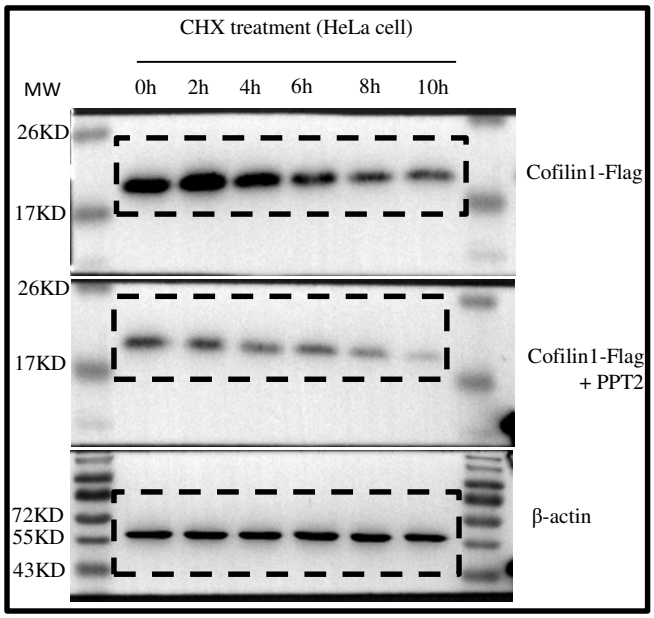
Uncropped blot of Fig.3D



Uncropped blot of Fig.3C



Uncropped blot of Fig.3E



Uncropped blot of Fig.3H

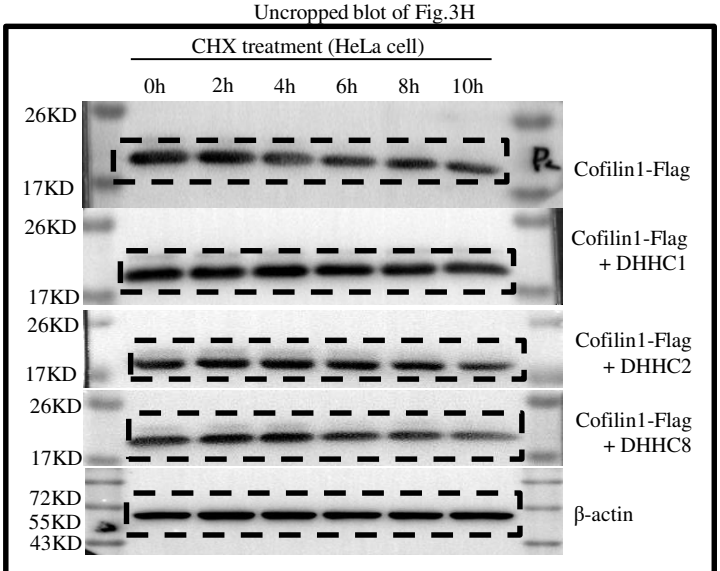
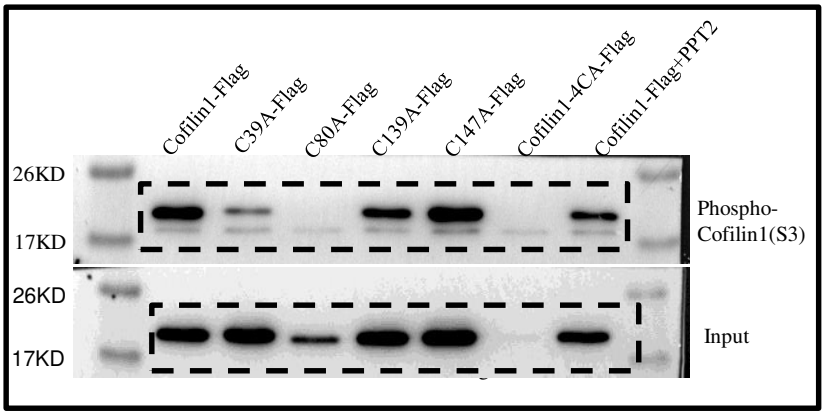
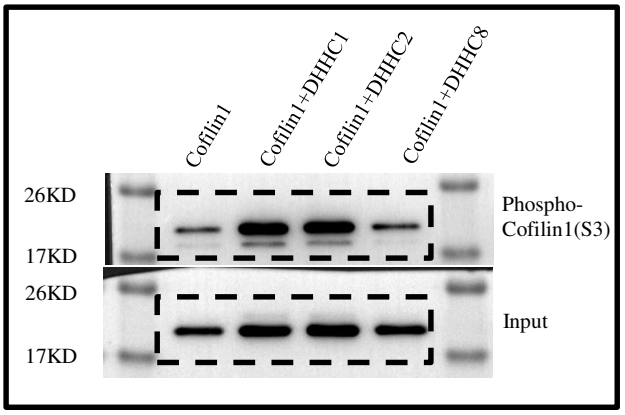


Fig. S14

Uncropped blot of Fig.4A



Uncropped blot of Fig.4E



Uncropped blot of Fig.4G

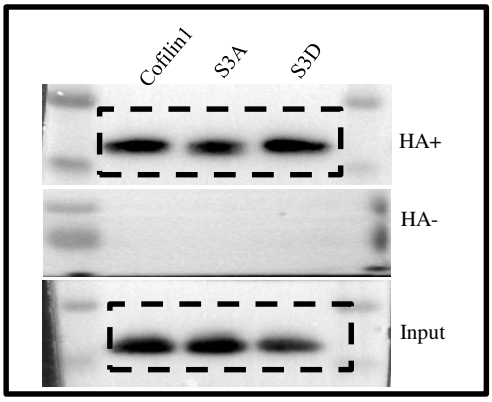
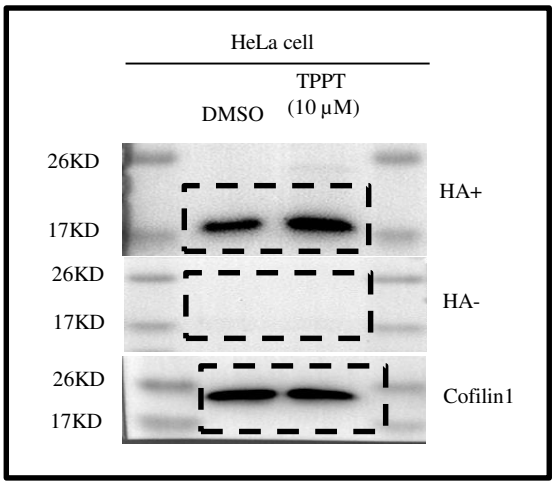
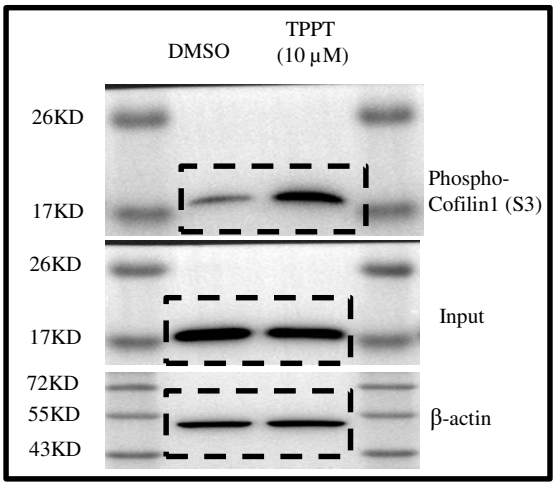


Fig. S15

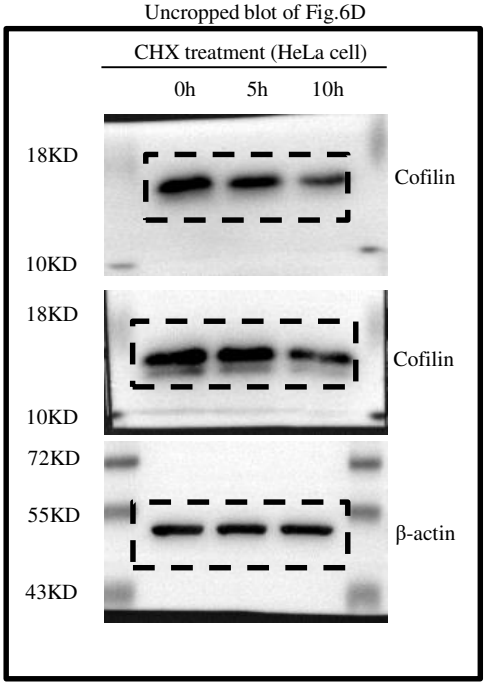
Uncropped blot of Fig.6B



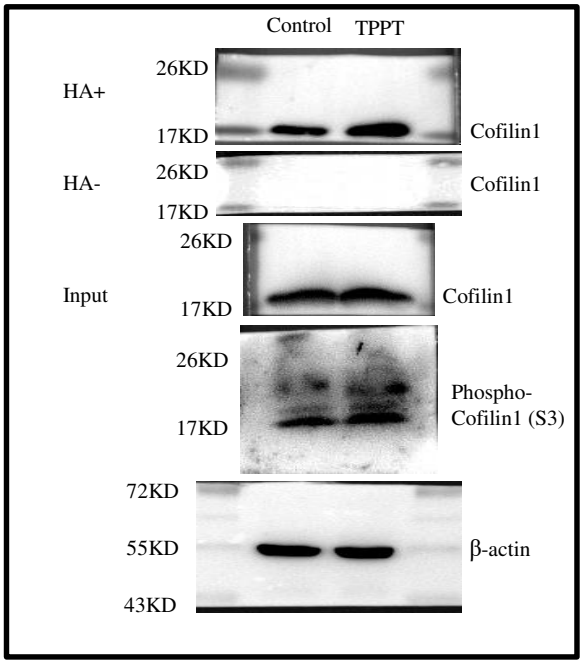
Uncropped blot of Fig.6C



Uncropped blot of Fig.6D



Uncropped blot of Fig. 7C



Supplementary Files

This is a list of supplementary files associated with this preprint. Click to download.

- UncroppedWB.pdf